

# Scaled testing of maximum-reserve active power control

Simone Tamaro, Davide Bortolin, Filippo Campagnolo, Franz V. Mühle, and Carlo L. Bottasso

Wind Energy Institute, Technical University of Munich, 85748 Garching b. München, Germany

**Correspondence:** Carlo L. Bottasso (carlo.bottasso@tum.de)

## Abstract.

We present the scaled experimental validation of an active power control (APC) algorithm designed to optimize the tracking accuracy of a wind farm in the presence of turbulent wind lulls. This is obtained by maximizing the minimum local power availability (called reserve) across the farm. This method combines an offline-computed open-loop setpoint scheduler aimed  
5 at the power reserves, with a fast closed-loop corrector tasked with enhancing tracking accuracy. The open-loop component is synthesized using an augmented engineering wake model, which captures the combined effects of yaw misalignment and power curtailment, wind tunnel-specific inflow characteristics, and the influence of the chord-based Reynolds number (caused by the small size of the models) on the performance of the rotors.

A preliminary simulation-based steady-state analysis indicates that the approach effectively enhances local power availabil-  
10 ity across the wind farm by leveraging both induction and wake steering control. The methodology is then experimentally demonstrated in a large boundary-layer wind tunnel with minimal blockage, in different scenarios, including dynamically varying wind direction conditions. Its performance is benchmarked against three alternative APC strategies sourced from the literature. During the experiments, the APC algorithms run in real time on a dedicated cabinet and communicate with the turbine controllers via a dedicated network. Dynamic wind direction changes are generated using a large turntable driven by a  
15 field-recorded wind direction time series, scaled to match the temporal dynamics of the wind tunnel.

Results show that in both static and dynamic scenarios, the proposed control strategy outperforms the reference methods in power tracking accuracy, particularly under high power-demand conditions, while maintaining a limited impact on structural fatigue. Notably, the algorithm effectively manages wake interactions and redistributes local power demands to increase local power reserves, thereby mitigating saturation effects and improving overall tracking performance.

## 20 1 Introduction

Active Power Control (APC) is a key area of wind farm control that has attracted a growing interest in the context of the ongoing energy transition (Aho et al., 2012; Ela et al., 2014). In regions with high wind energy penetration, wind farms are increasingly required to contribute to grid stability (Boyle and Littler, 2024). This can be accomplished at different time scales that span from the order of seconds (inertia control and primary frequency control) to minutes (secondary frequency control).  
25 In the secondary frequency control regime, a wind farm must adjust its total power output according to the requests of the transmission system operator (TSO) (Aho et al., 2012).

In recent years, extensive research has focused on developing wind farm control strategies aimed at increasing the collective power output of turbines. Common approaches include wake redirection (Jiménez et al., 2010; Campagnolo et al., 2016; Fleming et al., 2019; Doekemeijer et al., 2021; Nanos et al., 2022), static and dynamic induction control (Munters and Meyers, 2018; van der Hoek et al., 2019; Frederik et al., 2020b; Bossanyi and Ruisi, 2021), and, more recently, wake mixing (Frederik et al., 2020a; Mühle et al., 2024; Lin and Porté-Agel, 2024).

Wind farm active power control (APC), however, differs in a fundamental way from these power-boosting strategies. In fact, wind farms performing APC are required to operate in curtailed mode, producing less than the maximum power that they could generate in the present ambient conditions. This mode of operation introduces new control challenges. For instance, how should a turbine be controlled to curtail its power output? How is its wake affected by power curtailment, and can turbines be controlled collectively to benefit power tracking accuracy? Is the effectiveness of wake redirection methods modified by off-rated operation? And what are the consequences in terms of structural fatigue?

Some of these and other questions have already been addressed in the literature. For example, Fleming et al. (2016) highlighted the limits of open-loop APC methods for wind farms, and van Wingerden et al. (2017) showed that a closed-loop control architecture can effectively reduce power tracking errors. Gonzalez Silva et al. (2022) later extended this work and stressed the importance of addressing saturation events (i.e. conditions in which the local power demand exceeds the local power availability) to avoid negatively affecting power tracking accuracy. Vali et al. (2019) demonstrated the pairing of power tracking with a side goal, and specifically with the limitation of structural fatigue. The authors achieved this result by adopting a special power-demand distribution across the farm, and demonstrated their approach with actuator-disk large eddy simulations (LES). More recently Starke et al. (2023) and Oudich et al. (2023) have paired APC with wake steering, showing that the time scales required by wake redirection are compatible with secondary grid frequency regulation. However, these studies lack a comprehensive modeling of misaligned operation conditions – which are significantly affected by curtailment (Cossu, 2021; Heck et al., 2023) – and a dynamic analysis of wind direction variability.

To the authors' knowledge, none of the APC methods developed so far directly accounts for the power reserve available at each turbine, defined as the difference between the demanded power and the locally available one. When this reserve becomes small, turbines are more likely to experience saturation events, which degrade the ability of the wind farm to track power references. To address the need to mitigate the onset of saturations, Tamaro et al. (2025b) developed a maximum-reserve APC approach that explicitly maximizes the minimum reserve across the wind farm, thereby improving its ability to track power references while limiting local saturation events. In particular, when combined with wake steering, the additional power unlocked by the redirection of wakes is strategically converted into a directly usable and controllable reserve, which enlarges the admissible operating region for accurate tracking. This is particularly relevant in industrial delta-control operation (Aho et al., 2012), where power references and remuneration are defined relative to the greedy available power of the farm, so that increasing available power directly translates into increased reserve margins.

The primary goal of this paper is to provide a thorough scaled experimental demonstration of the maximum-reserve APC method of Tamaro et al. (2025b), by considering the metrics of tracking performance, saturation events, turbine loading, and actuator duty cycle.

In fact, so far most work on APC has been carried out numerically, and the experimental demonstration of this important wind farm control technology is still lagging behind. Two instances of experimental APC tests have been presented by Petrović et al. (2018) and Gonzalez Silva et al. (2024). Petrović et al. (2018) considered a small cluster of two rotors in two wind direction scenarios. Their study demonstrated the strong effects played by the power share distribution on tracking accuracy and structural fatigue, and by wake effects, especially in partial rotor overlap conditions. In their work, the flow was almost laminar and the turbines relied only on torque control to curtail their power output, which is not necessarily realistic. Gonzalez Silva et al. (2024) later considered a cluster of three turbines in full alignment conditions and tested two APC techniques. The authors showed the importance of saturation events in determining tracking accuracy, and highlighted the limits of load-balancing approaches in high power-demand conditions. That same paper also investigated two distinct wind turbine control approaches for off-rated operation, resulting in different wake characteristics, which in turn affect the local power availability at downstream rotors.

However, neither experimental nor numerical APC studies have yet accounted for wind direction variability. This is an important gap, as wind direction changes occur naturally in any wind farm site and heavily influence wake-rotor interactions (Porté-Agel et al., 2013).

It is yet another goal of this paper to experimentally characterize the method of Tamaro et al. (2025b) in realistic stationary and dynamic wind direction conditions. We achieve this by using a cluster of scaled wind turbines operating in a large boundary-layer wind tunnel, where varying wind directions are used to replicate some of the dynamic effects happening in the field. By exploiting the fact that time flows much faster in a scaled experiment than at full scale (Canet et al., 2021; Bottasso and Campagnolo, 2022) – with a speedup larger than 80 in the present case – this work overcomes the limited duration of the simulations in our previous numerical study. The wind tunnel campaign presented in this work improves on some preliminary tests that we reported in Tamaro et al. (2024b). Compared to that work, here we have extended the operating conditions, refined the APC algorithms, and expanded the analysis of the results with additional metrics, which now include saturation events and structural fatigue.

The paper is organized as follows: Sect. 2 briefly reviews the formulation of the maximum-reserve controller and of three additional APC methods for performance comparisons, Sect. 3 describes the experimental setup, and Sect. 4 details the steady-state simulation environment used to synthesize the controller setpoints. Experimental results are reported and discussed in Sect. 5 for scenarios with fixed wind directions, and in Sect. 6 for dynamic wind direction conditions. Finally, Sect. 7 draws conclusions and offers an outlook towards future work.

## 2 Active power control formulation

### 2.1 Closed-loop with maximum reserve (CL + MR)

The maximum-reserve APC used in this work has been extensively described in Tamaro et al. (2025b), so here we only summarize its main features. The core of the wind farm control architecture is an open-loop model-based setpoint optimal scheduler that determines the yaw misalignment and power demand of each turbine, given the power demand required by the

95 TSO and the ambient conditions. Furthermore, a feedback loop serves the purpose of correcting tracking errors that may arise from the open loop in real time. A sketch of the controller is shown in Fig. 1.

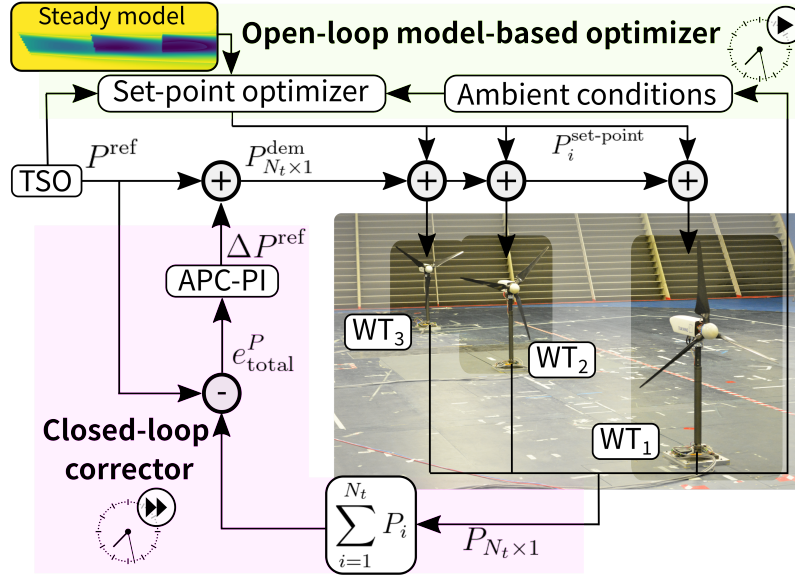


**Figure 1.** Schematic representation of the maximum-reserve APC controller, featuring an open-loop model-based optimizer and a closed-loop corrector.

The closed and open loops are executed at two distinct time rates, since their outputs involve physical phenomena characterized by different time scales. Specifically, the open loop updates the yaw setpoints  $\gamma_i$  and the power demand  $P_D$  at a slow pace, due to the time required by wakes to propagate downstream, whereas the closed-loop corrector acts at a rate that is two orders of magnitude faster.

### 2.1.1 Open-loop setpoint optimal scheduler

The open-loop component of the algorithm provides the optimal setpoints in terms of yaw misalignment and power share. These are computed by a gradient-based optimization that maximizes the smallest power reserve within the farm for a given overall power demand and ambient conditions.

105 Given the total number of turbines  $N$  in the farm, the power of the  $i$ -th machine is noted  $P_i = P_i(\mathbf{A}_i, \mathbf{u}_i)$ , where  $\mathbf{A}_i$  indicates the ambient conditions. Ambient conditions here are assumed to include freestream wind speed  $U_\infty$ , wind direction  $\psi$ , vertical shear  $k$ , and turbulence intensity (TI)  $I$ . The control inputs are noted  $\mathbf{u}_i$ , and they include the power share  $\alpha_i = P_i / \sum_{i=1}^N P_i$  and yaw misalignment  $\gamma_i$ .

The maximum power that can be generated by turbine  $i$  by adjusting its control setpoints  $\mathbf{u}_i$  (while keeping the setpoints of the other turbines fixed) in the ambient conditions  $\mathbf{A}_i$  is computed as

$$P_{a,i} = \max_{\mathbf{u}_i} P_i(\mathbf{A}_i, \mathbf{u}_i) = \frac{1}{2} \rho \pi R^2 U^3 C_P \eta_P(\gamma_i, \delta_i),$$

where  $\rho$  is the air density,  $C_P$  is the power coefficient,  $R$  is the rotor radius,  $U$  is the local rotor-equivalent wind speed, and  $\eta_P$  is the power scaling factor used by Tamaro et al. (2024a) to model power losses due to yaw  $\gamma$  and tilt  $\delta$ . The local flow conditions at the rotor of a turbine, including  $U$ , are computed with an engineering flow model, here based on FLORIS (National Renewable Energy Laboratory, 2022). The use of a steady-state flow model is justified by the fact that – as also shown later in Sect. 3.2 – the wind direction time scales targeted by the controller are one order of magnitude larger than the propagation time of wake effects.

The power tracking method looks for the combination of setpoints that produce the minimum possible maximum power ratio  $P_i/P_{a,i}$  across all  $N$  turbines in the farm while satisfying the power demand of the TSO,  $P_{\text{ref}}$ . This tracking criterion can be expressed as

$$\min_{\mathbf{u}} \max_{i \in [1, N]} \frac{P_i}{P_{a,i}}, \quad (1a)$$

$$\text{such that: } \sum_{i=1}^N P_i = P_{\text{ref}}. \quad (1b)$$

In fact, the smaller the power ratio  $P_i/P_{a,i}$ , the larger the reserve  $1 - P_i/P_{a,i}$  that is available to compensate against drops in the wind.

CL+MR improves tracking performance because it explicitly targets small reserves, which – when they are exhausted and generate saturations – are the main drivers of tracking deviations (Tamaro et al., 2025b). This formulation can be implemented by using induction control alone or in combination with wake steering, the latter case being considered here.

Equation (1) represents a constrained optimization problem. The optimization does not need to be performed in real-time during operation. Rather, it is executed offline for a set of ambient conditions and levels of wind farm curtailment. Results are collected in a lookup table (LUT), which is then interpolated at runtime, similarly to what is routinely done for power-boosting wind farm control (Meyers et al., 2022), so that

$$\alpha_i = \alpha_i(P_{\text{ref}}, \psi, U_{\infty}, k, I), \quad (2a)$$

$$\gamma_i = \gamma_i(P_{\text{ref}}, \psi, U_{\infty}, k, I). \quad (2b)$$

### 2.1.2 Closed-loop corrector

The closed-loop corrector is directly taken from the work of van Wingerden et al. (2017). The corrector consists of a simple proportional-integral (PI) feedback loop that operates on the power tracking error, which arises from the open-loop component of the control structure. Its goal is to ensure that – as some turbines deviate from their respective demands – the reference power tracking signal is promptly corrected.

The tracking error  $\Delta_P$  is defined as

$$140 \quad \Delta_P = P_{\text{ref}} - \sum_{i=1}^N P_i. \quad (3)$$

The control signal  $P_{\text{ref}}^{\text{PI}}$  at time instant  $\tau$  is defined as

$$P_{\text{ref}}^{\text{PI}} = K_{\text{APC}}^P \Delta_{P,\tau} + K_{\text{APC}}^I \sum_{j=1}^{\tau} \Delta_{P,j}, \quad (4)$$

where  $K_{\text{APC}}^P$  and  $K_{\text{APC}}^I$  are the PI gains, and  $j$  a time step counter. The wind farm is then required to track  $P_{\text{ref}} + P_{\text{ref}}^{\text{PI}}$ .

The PI gains are obtained with a tuning procedure based on the simple SIMULINK (The MathWorks, Inc., 2022) model  
 145 described in Sect. 3.4. The controller features an anti-windup element on the integrator when all turbines are saturated, i.e. when  $S = N$ , where  $S$  denotes the number of saturated rotors. Furthermore, the integrator is reset in certain conditions, as described in Sect. 3.4. The gain scheduling based on the number of saturated turbines proposed by van Wingerden et al. (2017) is not used due to the small size of the farm considered here, which causes abrupt variations in the gains that can lead to instabilities. Instead, when a turbine saturates, its local power tracking error is redistributed equally among the non-saturated  
 150 ones as proposed by Vali et al. (2019) and described in more detail in Sect. 2.4.

## 2.2 Reference APC formulations for performance comparison

We rely on three reference wind farm APC controllers to compare the performance of the maximum-reserve method, namely:

- **Open-loop (OL)**: this simple approach assigns predetermined setpoints  $\alpha_i$  to each turbine, as fractions of the power demanded by the TSO, so that  $\sum_{i=1}^N \alpha_i = 1$ . The setpoints  $\alpha_i$  are scheduled with the instantaneous wind direction, so  
 155 that  $\alpha_i = \alpha_i(\psi)$  to account for different local power availabilities induced by wake impingements. The values  $\alpha_i$  are computed with the FLORIS model (National Renewable Energy Laboratory, 2022), as described in Sect. 4.
- **Closed-loop (CL)**: this method is the same as OL with the addition of the closed-loop PI corrector described in Sect. 2.1.2. Similarly to the OL method, the values  $\alpha_i$  are scheduled with the instantaneous wind direction based on predictions from FLORIS.
- **Closed-loop with load balance (CL + LB)**: this method consists of CL without the fixed scheduling of the power share  
 160 setpoints  $\alpha_i$ . Instead, an additional PI loop is nested to distribute the setpoints  $\alpha_i$  with the goal of balancing loads within the wind farm (Vali et al., 2019). This coordinated load distribution (CLD) loop modifies the power share setpoints to minimize the load-balancing error  $\Delta_L$ , which is defined as

$$\Delta_{L,i} = L_i - \bar{L}, \quad (5)$$

165 where  $L_i$  is the load of the  $i$ -th turbine and  $\bar{L} = \frac{1}{N-S} \sum_{i=1}^{N-S} L_{i,\text{non sat}}$  is the average load in the farm. A PI power share distribution at time instant  $\tau$  is computed as

$$\alpha_{i,\tau} = K_{\text{CLD}}^P \Delta_{L,i} + K_{\text{CLD}}^I \sum_{j=1}^{\tau} \Delta_{L,i,j}, \quad (6)$$

where  $K_{CLD}^P$  and  $K_{CLD}^I$  are the PI gains.

170 In this work, the tower base fore-aft bending moment is chosen as the target load  $L$ . The PI gains of the CLD loop are tuned with the same SIMULINK model used for the APC loop, described in Sect. 3.4. As proposed by Gonzalez Silva et al. (2022), the mean load is computed considering only non-saturated turbines. Furthermore, the integrator is reset on all turbines in the event that all turbines reach saturation. In these conditions, the error  $\Delta_{L,i}$  is null – since it is computed only with non-saturated turbines – and the integrator component lies at zero, until at least one turbine recovers from saturation. An anti-windup is finally added to the integrator of each turbine whenever the power share  $\alpha$  exceeds  
175 unfeasible values.

It is important to mention that the setpoints for CL+MR are computed using the same FLORIS version adopted for OL, CL, and CL+LB. This ensures that any discrepancy deriving from the steady state model is present in each compared control approach. Furthermore, CL, CL+LB and CL+MR feature the same PI control block described in Sect. 2.1.2, ensuring that the closed-loop element is also the same.

### 180 2.3 Wind turbine controller

The wind turbine controller is based on two regimes, namely *below rated* and *rated*. In below rated conditions, blades lie at the optimal pitch angle, while the generator torque is scheduled with the rotor speed  $\Omega$  to ensure that the tip speed ratio  $\lambda$  yields the maximum  $C_P$ . The rated condition occurs when  $\Omega$  exceeds its rated value  $\Omega_R$ . In this case, torque is fixed while pitch angle increases from its optimal value to limit the power output to  $P_R$ . Turbines can track a given power demand  $P_D$  (where  
185  $P_D \leq P_R$ ) by adjusting  $\Omega_R$  and by setting  $Q_R = P_D/\Omega_R$ .

In this control strategy, the blade pitch angle  $\theta$  serves as an indicator of the operating reserve – or margin – for a curtailed wind turbine (Tamaro and Bottasso, 2023). Typically, larger values of  $\theta$  suggest a greater margin, as the turbine is functioning below its optimal power coefficient. The minimum (so called “fine”) value for  $\theta$  corresponds to the optimal pitch angle  $\theta_{opt}$ , which achieves the maximum  $C_P$ .

190 This controller was selected here because it directly accepts a power-demand input and uses the blade pitch angle to accurately follow it. Alternative control strategies could also be implemented, though they might lead to different APC performance.

### 2.4 Identification and treatment of saturation conditions

Saturations are detected on one turbine when the blade pitch lies at its optimal value plus a tolerance, and the tracking error exceeds a given threshold as specified in Sect. 3.1. When a wind turbine enters saturation, its power demand is set to  $P_{D,i}^*$ ,  
195 which is the last value recorded before saturation, and its power share is computed as

$$\alpha_i = \frac{P_i}{P_{ref} + P_{ref}^{PI}}. \quad (7)$$

Then its local tracking error is equally redistributed to non-saturated turbines in the form of an additional power demand, in order to ensure that  $\sum_{i=1}^N \alpha_i = 1$ . Notice that local isolated persistent saturation events do not necessarily introduce significant tracking errors as long as other turbines have enough margin to compensate.

200 Clearly, conditions in which all wind turbines are close to saturation are particularly harmful to the tracking accuracy, as a cascading effect can be triggered that may lead to all turbines being saturated. In this case, all wind turbines operate in greedy mode, and if the TSO demand drops, a large negative  $\Delta P$  will result. To avoid this situation, when the wind farm produces more than the instantaneous demand (with a threshold, as explained earlier), every saturation condition is forcibly reset.

### 3 Methods

#### 205 3.1 Experimental set-up

The wind tunnel experimental campaign is performed with a cluster of three G1 wind turbines (Bottasso and Campagnolo, 2022; Wang et al., 2021) – labeled  $WT_1$  (upstream),  $WT_2$  (center), and  $WT_3$  (downstream) – longitudinally spaced by  $5D$ , where  $D = 1.1$  m is the rotor diameter. The G1 scaled machine has a rated rotor speed  $\Omega_R$  of 850 RPM, a rated power  $P_R$  of 46 W, an optimal collective blade pitch angle  $\theta_{OPT}$  of  $0.43^\circ$ , and zero tilt. The time compression ratio is equal to about 80, 210 which means that time flows much faster in the experiment than at full scale (Canet et al., 2021; Bottasso and Campagnolo, 2022). Each G1 is real-time controlled by a dedicated Bachmann M1 PLC (Bachmann electronic GmbH, 2017), which executes the turbine-level controller described in Sect. 2.3 every  $\Delta t = 4$  ms. The maximum yaw rate is equal to  $20^\circ\text{s}^{-1}$ , corresponding to approximately  $0.25^\circ\text{s}^{-1}$  at full scale, which is a realistic value (Jonkman et al., 2009; Bortolotti et al., 2019).

Tests are performed in the atmospheric test section of the wind tunnel of the Politecnico di Milano (Bottasso et al., 2014) in 215 moderate turbulence conditions, with a power-law shear exponent  $k = 0.14$ , a TI  $I = 6\%$  at hub height, and an integral length scale of turbulence of  $0.79D$ . These ambient conditions are representative of offshore scenarios under neutral atmospheric boundary layer conditions. It is important to recall that even a fairly mild freestream turbulence intensity results in very large turbulent fluctuations at downstream turbines, especially in such closed spaced configurations; for example, Fig. 11 of Tamaro et al. (2025b) shows wake-affected turbines experiencing TI values exceeding 30% for a freestream TI of 5.7%. Such high 220 turbulence intensities create very challenging conditions for power tracking at downstream turbines.

The blockage ratio considering one G1 rotor is 1.8%, which is significantly smaller than previous APC wind tunnel studies (Petrović et al., 2018; Gonzalez Silva et al., 2024). The three turbines are installed on a large turntable. The rotational speed of the wind tunnel fans is kept constant during the experiments. The resulting wind speed  $U_\infty$ , measured by a Pitot tube placed  $4D$  upstream of  $WT_1$ , is approximately equal to  $5.5\text{ ms}^{-1}$ .

225 Two sets of experiments are conducted, respectively referred to in the following as “static” and “dynamic”.

In the static tests, the turntable is fixed at an angle  $\psi$  to reproduce a specific wind direction. Two angles are considered, corresponding to partial rotor overlaps of 75% ( $\psi = 2.8^\circ$ ) and 50% ( $\psi = 5.7^\circ$ ), respectively. We define rotor overlap as the fraction (in percentage) of the diameter that two wind turbine rotors share when looking downstream. An overlap of 100% corresponds to perfectly aligned rotors (center-to-center), while 50% overlap means that the downstream rotor is laterally 230 displaced by half a rotor diameter. In the static wind direction scenarios, each test has a duration of approximately 30 seconds, corresponding to about 4 hours at full scale. Six repetitions are performed to reduce the uncertainties caused by the turbulent fluctuations of the flow.

In the dynamic tests, the turntable is rotated according to a pre-determined time series, in order to dynamically vary the wind direction over the cluster of turbines. In this case, each test has a duration of 180 seconds, to match the overall duration of the static tests.

Figure 2 shows the wind tunnel setup, while Fig. 3 shows the vertical profiles of the mean streamwise velocity and turbulence intensity measured at the location of the upstream turbine  $WT_1$  for  $\psi = 0^\circ$ .

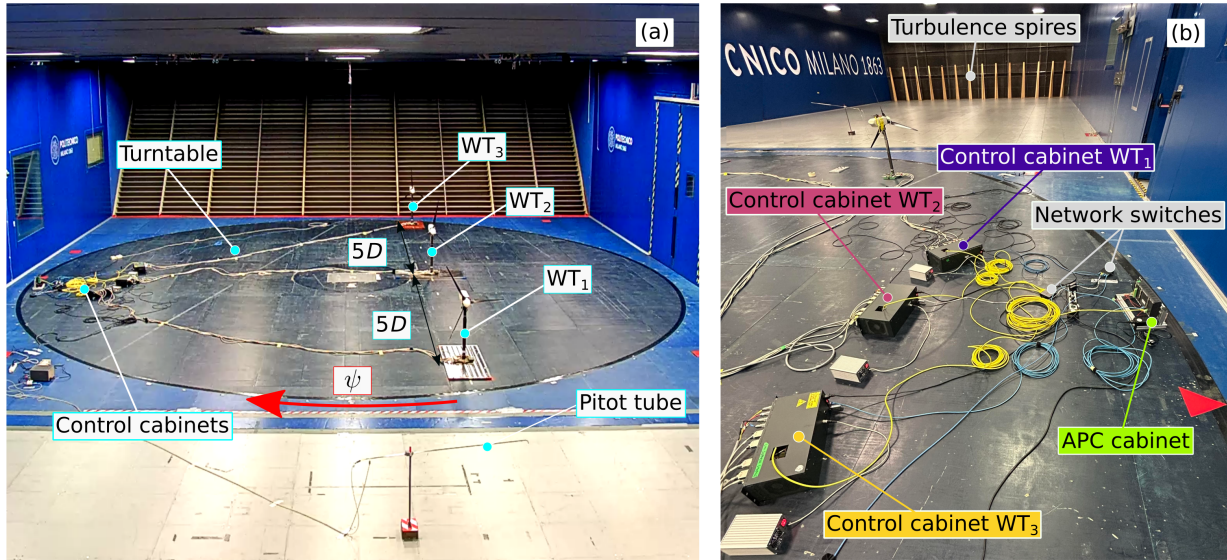


**Figure 2.** Wind tunnel setup (a) and closeup view of the control cabinets (b).

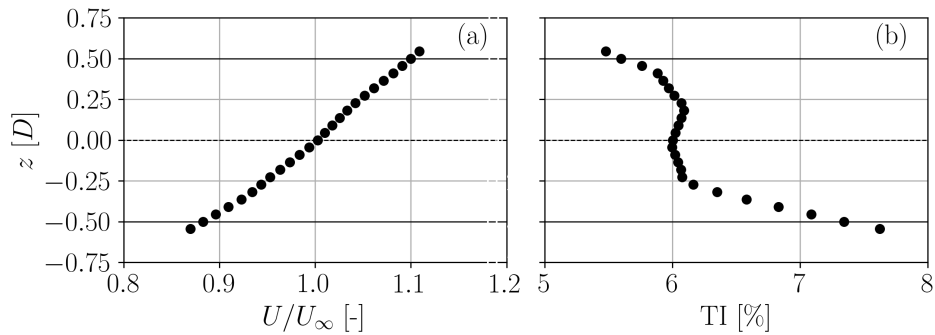


**Figure 3.** Wind tunnel inflow. Vertical wind speed profile (a); vertical TI profile (b).

The APC algorithms are implemented in MATLAB SIMULINK (The MathWorks, Inc., 2022), from which C++ codes are exported, and later compiled and loaded onto a Bachmann M1 PLC (Bachmann electronic GmbH, 2017). At every time step, the APC controller receives information on the current power demand and, for each wind turbine, on its instantaneous power production, blade pitch angle, and tower base fore-aft bending moment. Furthermore, the APC controller is also informed in

real-time about the current wind farm power demand  $P_{ref}$  and the current wind direction  $\psi$ . Within one sampling period, the setpoints of demanded power and nacelle yaw are computed by the APC controller and dispatched to each wind turbine. The direction of the wind relative to the farm is read from the turntable encoder. Therefore, its measurement can be considered exact up to the accuracy of this sensor. In the field, the knowledge of  $\psi$  is definitively more uncertain, due to the typically limited accuracy of the onboard anemometry system and the yaw encoder. The effects of wind direction uncertainties on wake steering performance were experimentally investigated by Campagnolo et al. (2020), using a very similar setup as the one considered here.

The control cabinets executing the wind turbine and APC controllers are connected to a PC in the control room via Ethernet. This PC is used to monitor the wind turbine sensors through a graphical user interface, to install and uninstall applications, to activate the wind farm controller, and to modify its settings as necessary. The Modbus communication protocol is used to start simultaneous data acquisitions, due to its compatibility with MATLAB. Communication between the APC and the wind turbine controllers is instead accomplished with Ethernet cables through the Profinet protocol (Profibus Nutzerorganisation e. V. (PNO), 2018). This system was chosen due to its relatively fast communication capabilities and integration with the existing setup. The APC algorithms are executed with a timestep of 4 ms (equivalent to approximately 0.3 s at full scale) to match the timestep of the wind turbine controllers. In CL+MR, the open-loop scheduler is updated 100 times slower, i.e. every 0.4 s, corresponding to approximately 30 s at full scale. A sketch of the connections among the various components of the system is shown in Fig. 4.

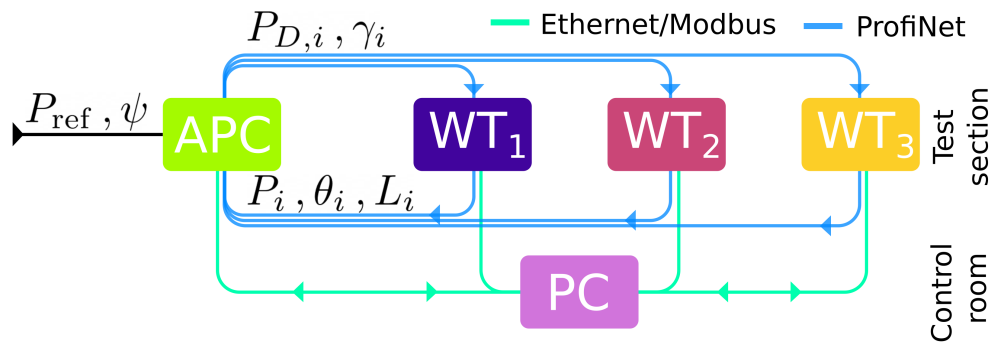


**Figure 4.** Sketch of the wiring connections among wind turbines, APC, and PC.

Local saturation conditions are indicated by a flag that is raised when both of the following conditions are simultaneously verified:

- the tracking error of a turbine exceeds 1% of the rated power  $P_R$ , i.e. 0.46 W, and
- its blade pitch angle is lower than  $\theta_{OPT} = 0.37^\circ$ .

Saturation conditions are also used to control the integral part of the APC PI controller. As discussed in Sect. 2.1.2, the integrator in the APC loop includes an anti-windup element that is activated when all turbines in the wind farm become saturated. This mechanism quickly reduces the integral term by applying to it a gain of 0.99 at each timestep.

All saturation flags are reset when the wind farm power output exceeds  $P_{\text{ref}}$  by more than  $3\%P_R = 1.38 \text{ W}$ . This mechanism addresses the situation in which all turbines become saturated. In such cases, the rotors are commanded to follow  $P_{D,i} = P_{D,i}^*$ , i.e. the last demanded power value prior to saturation, as described in Sect. 2.4. However, when all turbines are saturated, the system is unable to detect changes in  $P_{\text{ref}}$ . Consequently, the machines would continue tracking  $P_{D,i}^*$  even if  $P_{\text{ref}}$  decreases. To avoid this situation, the APC integrator and all saturations are reset whenever  $\Delta P < -3\%P_R$ . In the CLD PI controller, the integrator is reset either when all turbines become saturated or when this condition ends.

The control algorithms rely on multiple first-order filters. Cut-off frequencies are normalized using the rated rotor speed  $\Omega_R$ , which allows for a straightforward conversion to the full-scale case. For all controllers described in Sect. 2, the power generated by each turbine is low-pass filtered using a first-order transfer function with a cut-off frequency of 5 Hz ( $= 0.35\Omega_R$ ), before inputting it in the farm-level controller. A first-order filter is chosen here to limit the time delay associated with higher-order filters, which would hinder tracking accuracy. A cut-off frequency of 1.57 Hz ( $= 0.11\Omega_R$ ) is used to update the power setpoints, while a lower cut-off of 0.72 Hz ( $= 0.05\Omega_R$ ) is employed for the power demand. These different cut-off frequencies are selected to ensure that the power-demand signal remains smooth while minimizing delays in the setpoints.

For CL+LB, fore-aft bending moments are filtered using a moving average with a fundamental frequency of 1 Hz ( $= 0.07\Omega_R$ ). This value is one order of magnitude smaller than the turbine first fore-aft mode at 16 Hz, thereby ensuring that the controller detects only mean loads and does not react to structural vibrations.

### 3.2 Turntable control

The wind tunnel turntable has a diameter of 13 m, and it can be rotated to follow a prescribed time history (Campagnolo et al., 2020). The time series has been sampled at 1 Hz at an onshore test site in northern Germany (Bromm et al., 2018), and scaled by the speed-up factor of the experiment. Campagnolo et al. (2020) have extensively discussed this setup, showing a good agreement between the wind direction dynamics in the field and in the lab. Figure 5 reports the tunnel-scaled direction time history  $\psi(t)$ .

The figure shows that the scaled time history mainly consists of fluctuations characterized by slow frequencies  $f_\psi \leq 0.05 \text{ Hz}$ . These correspond to time scales longer than 20 seconds, which are one order of magnitude larger than the 1 to 2 seconds characterizing the propagation time of wake effects. Clearly, the same conclusions would apply at full scale. This also justifies the adoption of a steady-state wake model for the synthesis of the controller.

Throughout the experiment, the wind direction changes sign five times. This condition is particularly challenging when performing double-sided wake steering since it requires a sudden, large yaw angle variation to change the side where wakes are deflected.

Figure 6a presents the measured available farm power as a function of wind direction  $\psi$ , while Fig. 6b shows the measured variation of local power share as a function of  $\psi$  in the absence of wind farm control (i.e. in standard greedy mode).

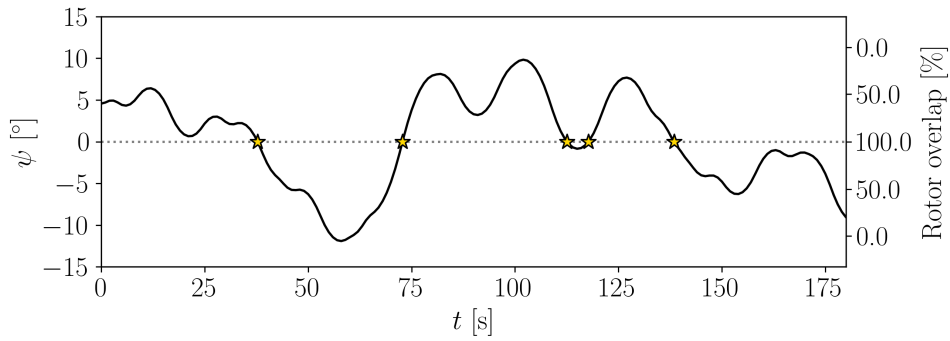


**Figure 5.** Time history of wind direction  $\psi(t)$ . Full rotor alignments ( $\psi = 0^\circ$ ) are highlighted.

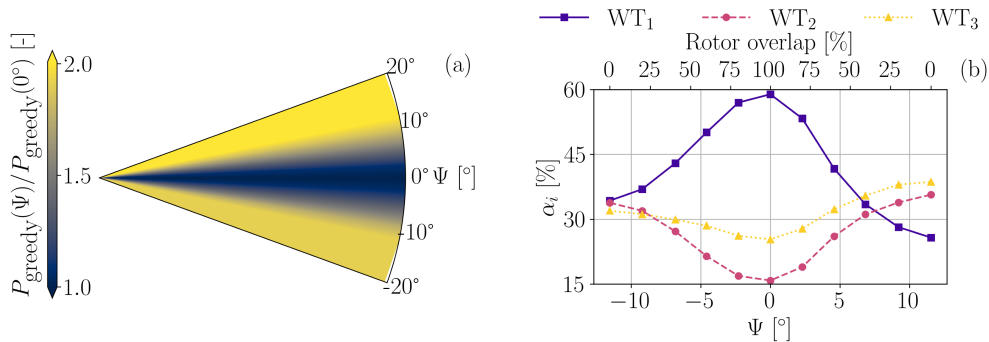


**Figure 6.** (a) Non-dimensional available power  $P_{\text{greedy}}(\psi)/P_{\text{greedy}}(0^\circ)$  as a function of wind direction  $\psi$ . (b) Local power setpoints as functions of  $\psi$  in greedy mode. When  $\psi = 0^\circ$ , the wind turbines are fully aligned.

Figure 6a highlights the strong effect of wake impingement on power production. The minimum available power is visible in correspondence with  $\psi \approx 0^\circ$ . The lack of symmetry with respect to  $\psi$  is due to a lateral inhomogeneity of the flow within the wind tunnel (Campagnolo et al., 2020). Overall, WT<sub>2</sub> appears to be suffering the most significant power losses, as in fact it produces only 15% of the wind farm power when  $\psi = 0^\circ$ . WT<sub>3</sub> presents a slightly higher power due to the high turbulence in the two wakes that impinge on it, which speeds up their recovery.

### 3.3 Reference power-demand signal

A dynamic reference power signal typical of automatic generation control (AGC) is used as input signal to the farm-level tracking controllers. AGC is the secondary response regime of grid frequency control, and it consists of dynamically adjusting the power output of a plant according to the request of the TSO (Aho et al., 2012). A similar signal has been considered by other authors (Fleming et al., 2016; van Wingerden et al., 2017; Vali et al., 2019; Shapiro et al., 2017; Boersma et al., 2018).

The signal is defined as

$$P(t, \psi) = P_{\text{greedy}}(\psi) (b + cn_k^{\text{AGC}}(t)), \quad (8)$$

where  $n_k^{\text{AGC}}(t)$  is a normalized time-dependent test signal,  $P_{\text{greedy}}(\psi)$  is the available power of the wind farm in greedy aligned conditions at a specific wind direction  $\psi$ , and  $b$  and  $c$  are two parameters that respectively shift and scale  $n_k^{\text{AGC}}$ . 310

Due to the small size of the models, the original signal is accelerated in time by a factor of 81.73 (Bottasso and Campagnolo, 2022). Figure 7a shows  $n_k^{\text{AGC}}$  as a function of time. In the tests with the dynamic turntable, the reference power signal in Fig. 7a is looped multiple times for a total length of three minutes. In this case, the instantaneous available wind farm power  $P_{\text{greedy}}(\psi)$  depends on the instantaneous wind direction  $\psi$  as shown in Fig. 6a. Figure 7b shows the time history 315 of  $n_k^{\text{AGC}}(t)P_{\text{greedy}}(\psi)/P_{\text{greedy}}(0^\circ)$ , where both the full-scale (top  $x$  axis) and wind tunnel (bottom  $x$  axis) time scales are reported.

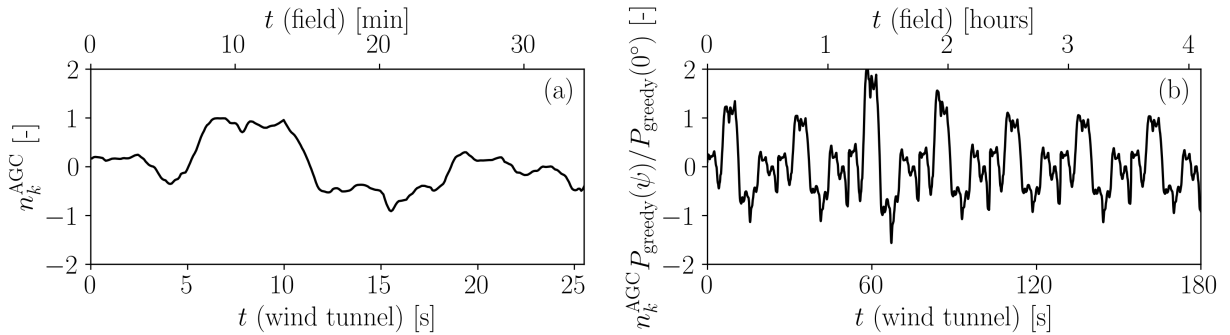


**Figure 7.** Time series of the reference test signal  $n_k^{\text{AGC}}$  (a), and of the normalized power reference used in the dynamic turntable experiments (b). The additional  $x$  axis on the top part of the plot indicates full-scale time.

The reference power signal is initialized with a rising ramp to reduce the effects of initial transients. Notice how a 4-hour-long test in the field is replicated in the significantly shorter time of 180 seconds in the wind tunnel. It is important to notice that the test time of 3 minutes covers 24 full-scale 10-minute turbulent realizations, which ensures the statistical convergence 320 of results (Liew and Larsen, 2022).

### 3.4 Tuning procedure of the PI gains

The gains used in the APC controllers and the cut-off frequencies of the filters are tuned using a digital twin of the wind tunnel setup. This model of the experiment is implemented in SIMULINK (The MathWorks, Inc., 2022) and includes three blocks representing the wind turbines, each running the same controller used in the wind tunnel tests. The drivetrain dynamics are modeled as described in Campagnolo et al. (2022a), while rotor aerodynamics are represented using LUTs computed offline 325 with a blade element momentum (BEM) model of the G1 (Wang et al., 2020). The LUTs schedule rotor thrust and torque as functions of turbine operating conditions. Tower dynamics are modeled with a second-order system.

The Jensen wake model (Jensen, 1983), combined with the instantaneous thrust coefficient  $C_T$ , is used to estimate the wake deficit for downstream turbines. A delay is used to simulate the time required for wake effects to propagate downstream.

330 The same CL and CL+LB controllers used in the wind tunnel experiments are included in the digital twin. To improve the robustness of gain tuning, zero-mean white noise with a variance of  $0.25 \text{ W}^2$  is added to the measured input power.

Gain optimization is performed with the goal of reducing the influence of saturation events, using a gradient-based interior-point algorithm with a power-demand signal characterized by  $P_{\text{greedy}} = 55 \text{ W}$ ,  $b = 0.8$ , and  $c = 0.1$ .

For the CL+LB controller, the cost function is defined as

$$335 \quad J = 0.75 \overline{\Delta}_P + 0.25 \sum_{i=1}^N \overline{\Delta}_{L,i}, \quad (9)$$

which represents a weighted sum of the non-dimensional tracking error  $\overline{\Delta}_P$  and the non-dimensional load-balancing error  $\overline{\Delta}_{L,i}$ . Both quantities are scaled to lie in the interval  $[0, 1]$ .

The resulting gains for the APC loop are

$$K_{\text{APC}}^P = 1.3127 \quad [-], \quad K_{\text{APC}}^I = 14.9253 \text{ s}^{-1} = 1.05 \Omega_R.$$

340 For the CLD loop, the gains are

$$K_{\text{CLD}}^P = 0.03427 \text{ Nm}^{-1} = 0.52 L_R^{-1}, \quad K_{\text{CLD}}^I = 0.07959 \text{ Nm}^{-1} \text{ s}^{-1} = 0.09 L_R^{-1} \Omega_R,$$

where  $L_R = 15.2 \text{ Nm}$  is the tower base fore-aft bending moment of the G1 turbine at rated wind speed.

#### 4 Steady-state performance characterization

The engineering farm flow model FLORIS v3 (National Renewable Energy Laboratory, 2022) is used here to perform a steady-

345 state characterization of the performance of the various controllers, before entering the wind tunnel. The same model is also used to synthesize the open-loop part of the controller, yielding the control LUTs.

The wake deficit and deflection models proposed by Bastankhah and Porté-Agel (2014) are employed, along with the turbulence model by Crespo and Hernández (1996). In both cases, the model parameters are fine-tuned to replicate wind tunnel conditions, as summarized in Appendix A.

350 FLORIS is also augmented with a heterogeneous wind map that replicates the asymmetric inflow of the wind tunnel shown in Sect. 3.2 (Campagnolo et al., 2022b), following the procedure proposed by von Braunbehrens et al. (2023). In OL and CL, the same engineering flow model is used to assign the power share setpoints  $\alpha_i$  as functions of  $\psi$ , given the ambient conditions of the experiments.

##### 4.1 Setpoints for CL+MR: combining wake steering with off-rated operation

355 In CL+MR, wind turbines are subjected to induction control and simultaneously perform wake steering. To model this combined off-rated and misaligned operation, LUTs of power coefficient  $C_P$  and thrust coefficient  $C_T$  are computed via an analyt-

ical model (Tamaro et al., 2024a). The adoption of such a model is motivated by the fact that off-rated operation spans a wide range of  $C_T$  values – and misaligned operation is strongly dependent on  $C_T$  (Cossu, 2021; Heck et al., 2023).

Another important aspect typical of scaled wind turbine models is the effect of the chord-based Reynolds number on the aerodynamic performance of the rotor (Bottasso and Campagnolo, 2022). This is relevant since with the controller described in Sect. 2.3, turbines operating in off-rated conditions experience low rotational speeds. These effects were taken into account by using a BEM model of the G1 that includes a dependency on the chord-based Reynolds number (Wang et al., 2020). Figures 8 and 9 show examples of LUTs for  $C_P$  and  $C_T$ , where the auxiliary factor  $\epsilon$  has been introduced to quantify the level of derating, with  $\epsilon = 1$  corresponding to the greedy power mode.

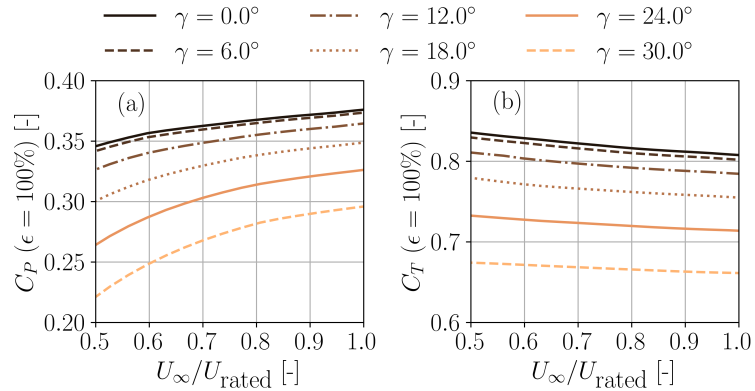


**Figure 8.** LUTs for (a) power coefficient  $C_P$  and (b) thrust coefficient  $C_T$  as functions of wind speed for the G1 turbine. Results corresponds to a power scaling factor  $\epsilon = 100\%$ , (i.e. no curtailment), and different yaw angles  $\gamma$ .

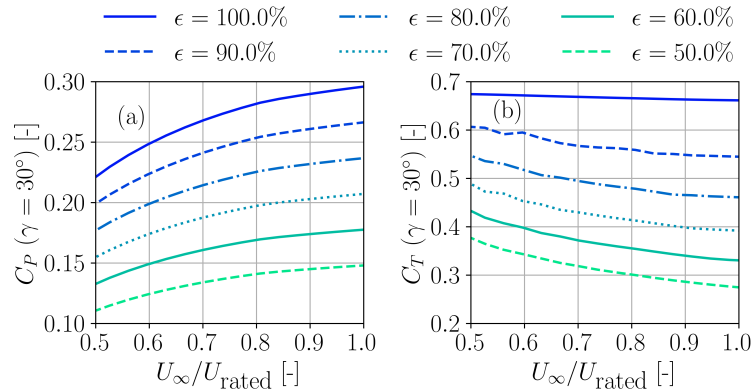


**Figure 9.** LUTs for (a) power coefficient  $C_P$  and (b) thrust coefficient  $C_T$  as functions of wind speed for the G1 turbine. Results correspond to a yaw angle  $\gamma = 30^\circ$  and different power scaling factors  $\epsilon$ , representing the level of power curtailment.

365 Since both power demand and wind direction vary, the LUTs for  $\gamma_i(P_D, \psi)$  and  $\alpha_i(P_D, \psi)$  are two-dimensional. Other model inputs, such as TI and inflow shear, are fixed as described in Sect. 3.1. To generate the LUTs, different optimizations are solved for each wind direction and wind farm power demand. When the optimization converges, the resulting power share setpoints are computed as  $\alpha_i = P_i / \sum_{i=1}^N P_i$ , and they are stored together with the yaw setpoints. The optimization problem is solved with the gradient-based Sequential Quadratic Programming (SQP) method (Brayton et al., 1979). With the aim  
 370 of avoiding entrapment in a local minimum, the optimization for the first power-demand level is carried out using various random perturbations of the power-boosting solution as initial guesses. After this first solution, the wind farm power demand is progressively lowered and the result of the previous optimization is used as starting guess for the next curtailment level. The minimum curtailment levels is limited to 40% of the maximum wind farm power, which is sufficient to cover the APC scenarios described in Sect. 3.3. Results are shown in Figs. 10 and 11 for the yaw and power setpoints, respectively.

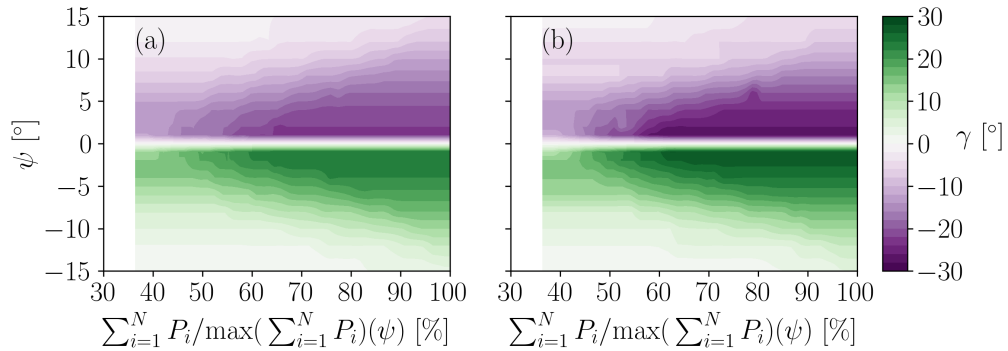


**Figure 10.** Optimal yaw setpoints  $\gamma$  that maximize the minimum power reserve for the experimental setup, plotted against the power demanded to the wind farm in percentage of the maximum power, and the inflow wind direction  $\psi$ . (a) WT<sub>1</sub>; (b) WT<sub>2</sub>.

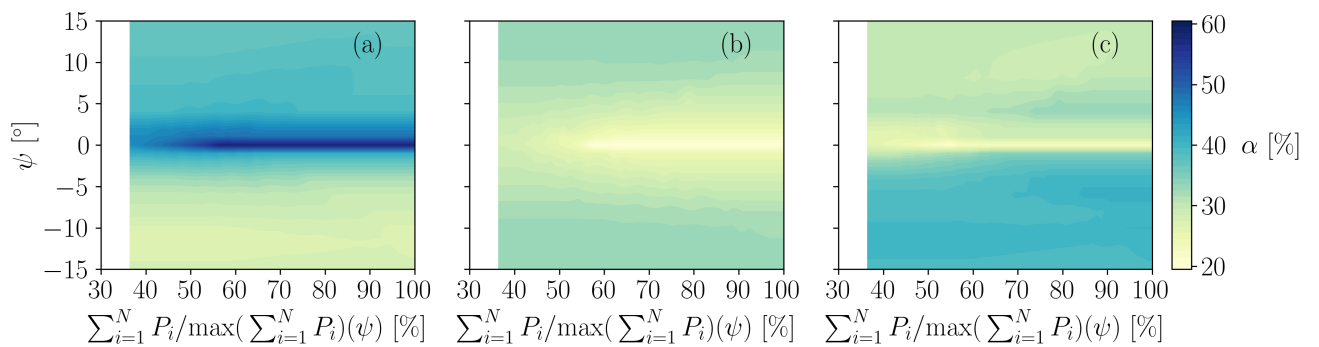


**Figure 11.** Optimal power setpoints  $\alpha$  that maximize the minimum power reserve for the experimental setup, plotted against the power demanded to the wind farm in percentage of the maximum power, and the inflow wind direction  $\psi$ . (a) WT<sub>1</sub>; (b) WT<sub>2</sub>; (c) WT<sub>3</sub>.

375 In the figures,  $\psi = 0^\circ$  represents a condition of precise alignment and therefore full wake impingement. Conversely, when  $0^\circ < |\psi| \leq 11.3^\circ$ , partial wake impingement occurs. The yaw setpoints present, in fact, a maximum absolute value in full waking, where steering is heavily used to increase power reserves. As  $\psi$  increases, the power setpoints start converging towards an equal power dispatch, i.e.  $\alpha_i = 1/N$ , while the yaw misalignment is progressively reduced. In fact, as  $\psi$  deviates away from  $0^\circ$ , wake impingement is less prominent, and all turbines perceive similar local inflow conditions.

380 The treatment of the  $\psi = 0^\circ$  condition is particularly relevant: under dynamic wind direction variations, when  $\psi$  switches sign, the upstream wind turbines must change their yaw setpoint by more than  $\pm 40^\circ$ . Delays in following this demand – which are expected due to the necessarily limited speed of the yaw actuation system – could result in relevant power losses, since the wake may be temporarily deflected towards downstream rotors, instead of away from them. To avoid this situation, no optimal wake steering is performed between  $-2^\circ < \psi < 2^\circ$ , but instead, the setpoints are interpolated from the values at  $\pm 2^\circ$  to ensure  
 385 a smooth transition when  $\psi$  switches sign. This solution should not result in a hindrance to the overall effectiveness of wake steering, since deflecting wakes is more effective in partial than in full impingement (Howland et al., 2019).

During operation,  $\alpha_i$  and  $\gamma_i$  are linearly interpolated from the LUTs in Figs. 10 and 11 based on the average power demand and wind direction computed over the previous 0.4 seconds. Clipping to the last available value of the LUT is used to avoid extrapolating.

## 390 4.2 Estimation of the power margins

The power reserves for CL + MR are compared to those of OL in steady-state conditions, using the simulation environment described earlier. The comparison considers the difference between the power produced  $P_i$  and the available power  $P_{a,i}$  for each turbine. Figure 12 shows the locally available power and the minimum power (last column) in the farm for two wind directions, i.e.  $\psi = 2.8^\circ$  and  $5.7^\circ$ , corresponding to partial rotor overlaps of 75% and 50%, respectively.

395 Results show that the largest wind farm power gain is obtained for  $\psi = 2.8^\circ$  ( $\approx +18\%$ ), followed by  $\psi = 5.7^\circ$  ( $\approx +14\%$ ), confirming that wake steering is particularly beneficial in partial wake impingement conditions (Howland et al., 2019). As a result of the higher wind farm power, a significant gain in power reserve is achieved with CL+MR relative to OL, in particular for the front turbine  $WT_1$ . This is favorable, since  $WT_1$  is often required to compensate for the saturations that may affect waked rotors. For these downstream turbines, the benefit of CL+MR becomes evident at severe power demands, i.e.  $\sum_{i=1}^N P_{i,OL} \approx$   
 400 95%, and it gradually decreases as  $\sum_i P_{i,OL}$  is reduced because of the loss of effectiveness of wake steering due to the lower operational  $C_T$  of upstream rotors. This, in fact, implies a lower velocity deficit in the wake and a less prominent deflection. Overall, CL+MR yields a distribution of power reserves across the turbines that is more uniform than when using the OL method, consistently with the goal of the optimization.

The last two plots on the right in Fig. 12 show the worst power reserve in each cluster across the range of wind farm power  
 405 demands, for the two considered wind directions. For OL,  $WT_1$  is the most critical rotor. Under curtailment, its power reserve increases linearly, albeit at a slower rate than that of the downstream rotors, which exhibit a nonlinear increase (as shown in the corresponding plots, appearing in the second and third column of the figure), likely due to wake effects. In contrast,

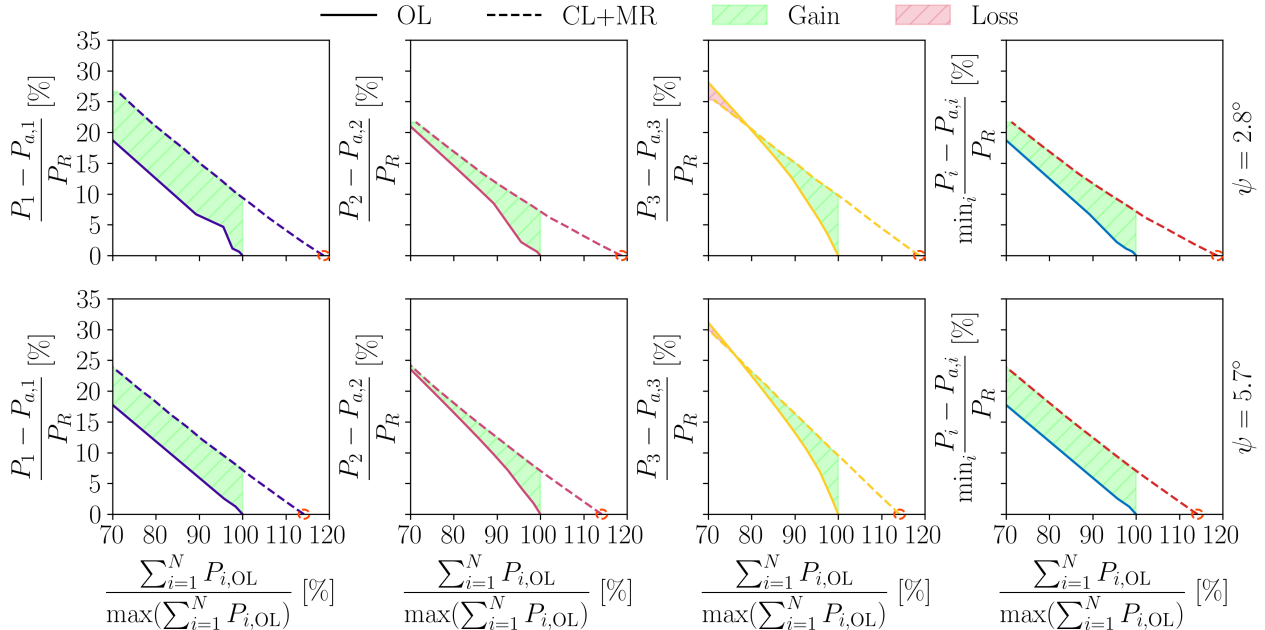


**Figure 12.** Locally available power normalized with the rated power  $P_R$ , obtained with a purely inductive wind farm control (labeled OL), and with the maximum-reserve strategy (labeled CL+MR) for  $\psi = 2.8^\circ$  and  $\psi = 5.7^\circ$ . (a) WT<sub>1</sub>; (b) WT<sub>2</sub>; (c) WT<sub>3</sub>; (d) minimum value in the wind farm. On the  $x$  axis, the wind farm power is normalized with its maximum value without wake steering. Red circles indicate the classical maximum power solution.

for CL+MR, the worst power reserve shifts from WT<sub>1</sub> to WT<sub>2</sub> as the rotors adjust their yaw alignment, in turn resulting in consistently larger margins than in the OL case.

## 410 5 Static wind direction experiments

In this section, we present the wind tunnel results for two fixed wind direction values equal to  $\psi = 2.8^\circ$  and  $5.7^\circ$ , corresponding to partial rotor overlaps of 75% and 50%, respectively.

### 5.1 Power tracking accuracy

#### 5.1.1 Wind farm tracking errors

415 Figures 13 and 14 present the root mean square (RMS) of the power tracking error recorded at the three power request levels  $b = 0.8, 0.85, 0.9$ , by each APC algorithm in the wind tunnel experiments. For each controller, six measurements are shown, indicating six repetitions, and whiskers indicate the mean RMS error and its uncertainty considering a 95% confidence level. Figure 13 presents the RMS of tracking error obtained for  $\psi = 2.8^\circ$ , while Fig. 14 refers to the case  $\psi = 5.7^\circ$ .

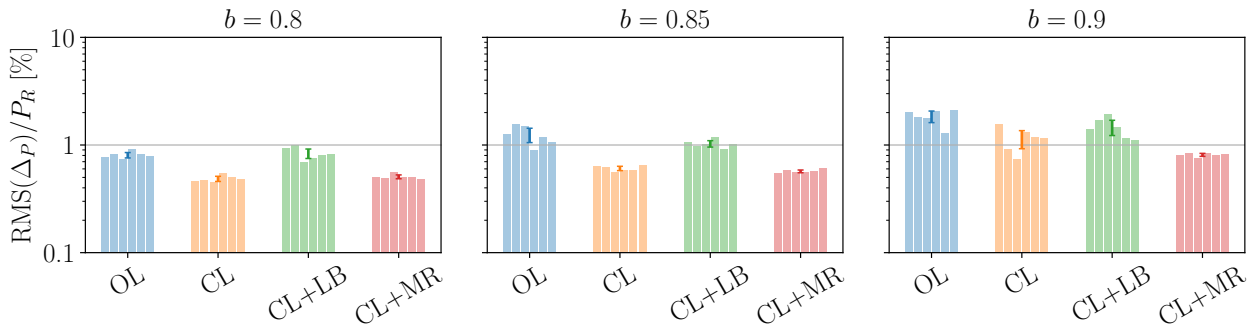


**Figure 13.** RMS of wind farm power tracking errors measured for the four APC algorithms and three power-demand levels  $b$ . Static experiment with fixed wind direction  $\psi = 2.8^\circ$ , corresponding to 75% rotor overlap. The results from six repetitions are reported with bars for each APC algorithm and power demand. Whiskers indicate 95% confidence intervals.

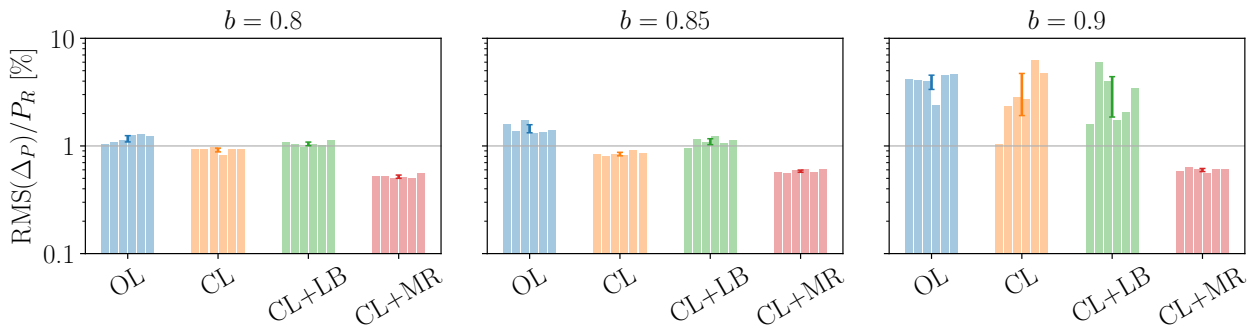


**Figure 14.** RMS of wind farm power tracking errors measured for the four APC algorithms and three power-demand levels  $b$ . Static experiment with fixed wind direction  $\psi = 5.7^\circ$ , corresponding to 50% rotor overlap. The results from six repetitions are reported with bars for each APC algorithm and power demand. Whiskers indicate 95% confidence intervals.

The plots show that the tracking error grows with the power request determined by parameter  $b$ . Closed-loop methods  
 420 reduce the tracking error consistently, with a generally larger effectiveness for  $\psi = 2.8^\circ$ , i.e. for the higher rotor overlap case. Interestingly, the variability of the results increases significantly as parameter  $b$  grows in all cases except for CL+MR. The smaller variability observed for CL+MR is likely due to larger power reserves, which reduce the likelihood of simultaneous saturation events that can dramatically affect tracking accuracy.

### 5.1.2 Wind turbine tracking errors

425 Figures 15 and 16 show the tracking RMS error of each wind turbine for various power-demand levels, for  $\psi = 2.8^\circ$  and  $\psi = 5.7^\circ$ , respectively.

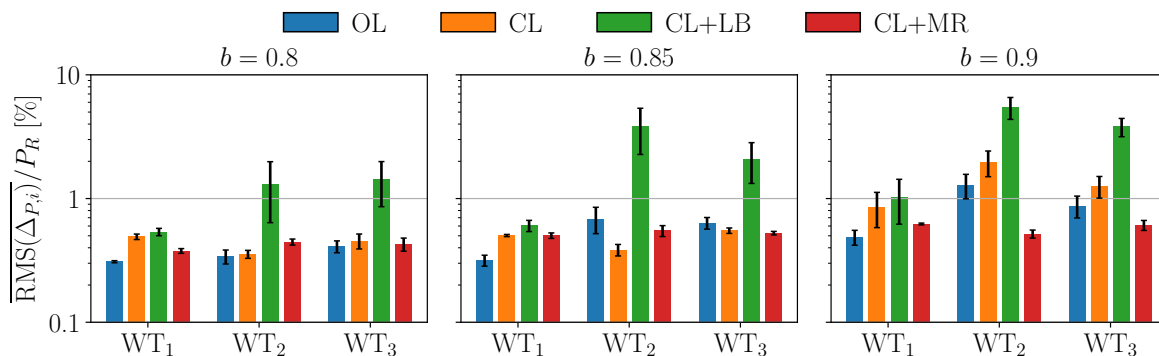


**Figure 15.** RMS of local power tracking errors for the four APC algorithms and three power-demand levels  $b$ . Static experiment with fixed wind direction  $\psi = 2.8^\circ$ , corresponding to 75% rotor overlap. Whiskers indicate 95% confidence intervals.

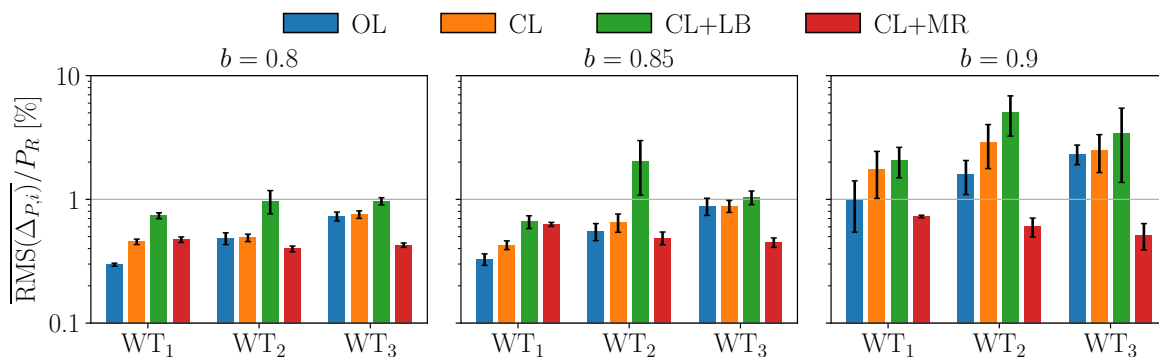


**Figure 16.** RMS of local power tracking errors for the four APC algorithms and three power-demand levels  $b$ . Static experiment with fixed wind direction  $\psi = 5.7^\circ$ , corresponding to 50% rotor overlap. Whiskers indicate 95% confidence intervals.

In the OL and CL+LB cases, waked rotors present the highest tracking error. In both cases, this is due to the generally low power reserves of waked rotors, which is exacerbated by the lack of a closed-loop for OL and by the coordinated load distribution for CL+LB. Compared to OL, CL increases the tracking errors of WT<sub>1</sub> because it calls this front turbine that is operating in freestream to compensate for the saturation of the waked turbines further downstream. CL+MR presents a consistently balanced error distribution. This is likely due to the rather uniform distribution of power reserves, which implies that all turbines have a similar likelihood of not being able to follow a local demand.

It should be remarked that for all methods except for OL, a saturated turbine will experience significant tracking errors. This does not necessarily imply a low wind farm tracking accuracy, but only as long as other turbines are able compensate. Therefore, it is important to ensure that local power reserves are not exhausted, which is precisely what the maximum-reserve formulation tries to accomplish.

## 5.2 Power reserve distribution

To quantify the mean power reserve of each turbine, we analyze the average collective blade pitch angle  $\bar{\theta}$ . With the controller described in Sect. 2.3, the closer  $\bar{\theta}$  is to the optimal pitch  $\theta_{\text{OPT}}$ , the less power reserve is available. Figures 17 and 18 show the local mean collective blade pitch angle for  $\psi = 2.8^\circ$  and  $\psi = 5.7^\circ$ , respectively.

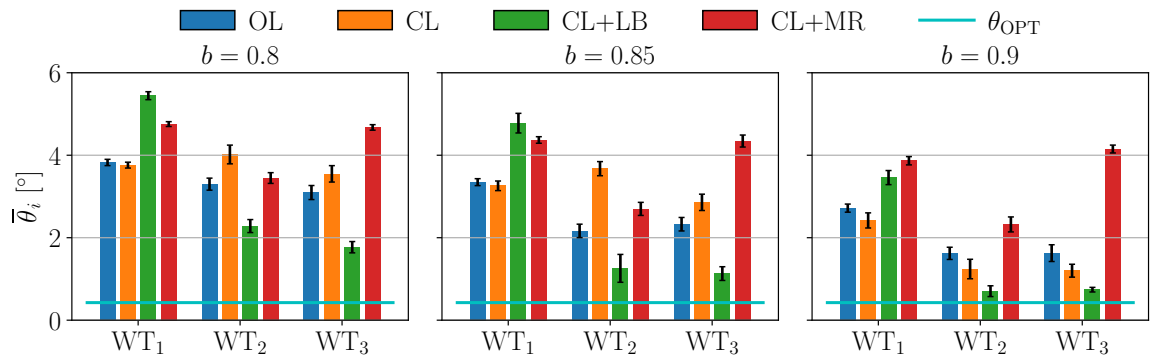


**Figure 17.** Local average blade pitch angle  $\bar{\theta}$  from the static turntable experiment for wind direction  $\psi = 2.8^\circ$ , corresponding to a 75% rotor overlap. Whiskers indicate 95% confidence intervals. Results are presented for three power-demand levels  $b$ .

Consistently with the tracking error analysis,  $\bar{\theta}$  appears to decrease as the power demand increases. OL and CL+LB present a power reserve distribution that is significantly unbalanced towards WT<sub>1</sub>. In particular, CL+LB presents the highest values of  $\bar{\theta}$  for WT<sub>1</sub>, but at the same time it also always yields low values of  $\bar{\theta}$  for waked rotors. CL remarkably improves the balancing of power reserves compared to OL, especially for  $\psi = 2.8^\circ$  and for low values of  $b$ . CL+MR presents a rather uniform distribution of the power reserves, favoring especially the most waked rotor, i.e. WT<sub>3</sub>. This directly confirms the effectiveness of wake steering, which, by laterally moving upstream wakes, improves the power reserve of the most downstream rotor.

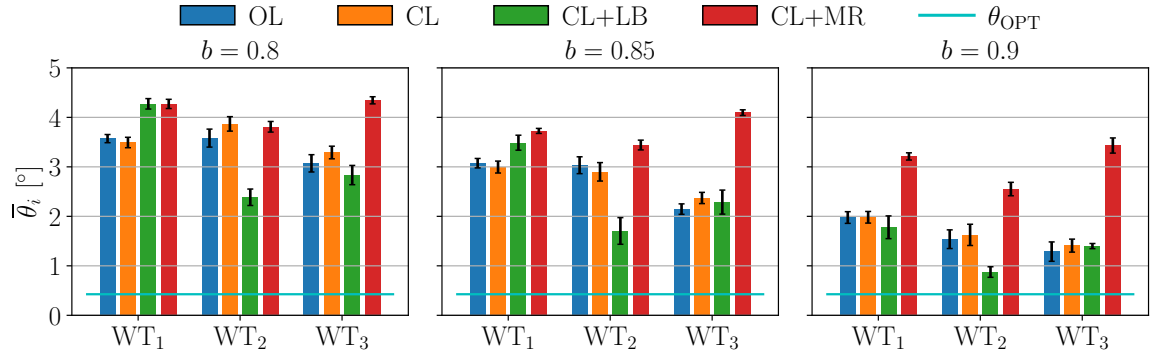


**Figure 18.** Local average blade pitch angle  $\bar{\theta}$  from the static turntable experiment with wind direction  $\psi = 5.7^\circ$ , corresponding to a 50% rotor overlap. Whiskers indicate 95% confidence intervals. Results are presented for three power-demand levels  $b$ .

### 5.3 Loads and fatigue

In the following loads and fatigue analysis, we only display data for the 75% rotor overlap scenario, since results for  $\psi = 5.7^\circ$  (50% rotor overlap) are similar (and reported, for completeness, in Appendix C).

450 The mean local load-balancing error of each rotor is shown in Fig. 19.

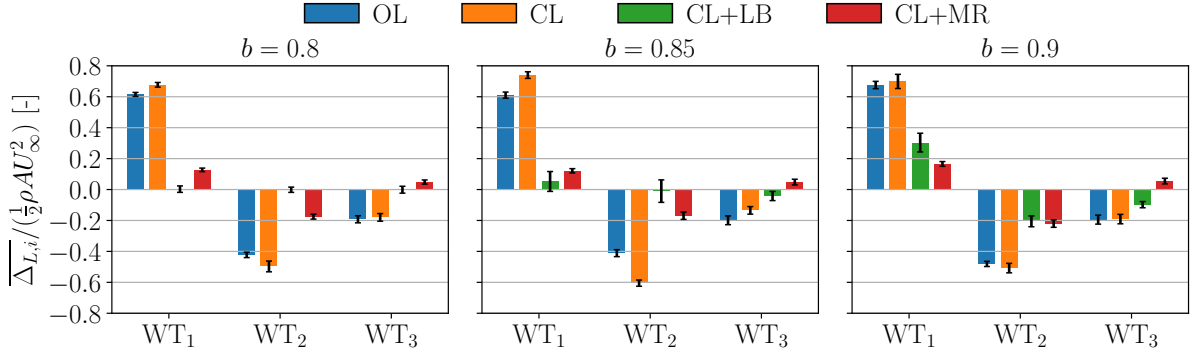


**Figure 19.** Mean local load-balancing error for the tower-base fore-aft bending moment for the static turntable experiment with wind direction  $\psi = 2.8^\circ$ , corresponding to a 75% rotor overlap.  $L$  is normalized by  $\frac{1}{2}\rho U_\infty^2$ . Positive values indicate loading above the wind farm average. Whiskers indicate the mean error over six repetitions and its uncertainty considering a 95% confidence level. Results are presented for three power-demand levels  $b$ .

Results show that for OL and CL, loading is maximum on WT<sub>1</sub> and decreases when moving downstream. CL+LB effectively balances loads in the wind farm, with remarkable effectiveness for  $b < 0.9$ . When  $b = 0.9$ , the significant increase in saturation

events is such that loads cannot be balanced anymore, since power tracking accuracy is prioritized. This shows the limit of the load-balancing strategy that, in some cases, is unable to achieve the goals for which it has been formulated.

455 Next, damage equivalent loads (DELs) at tower base are presented in Fig. 20.

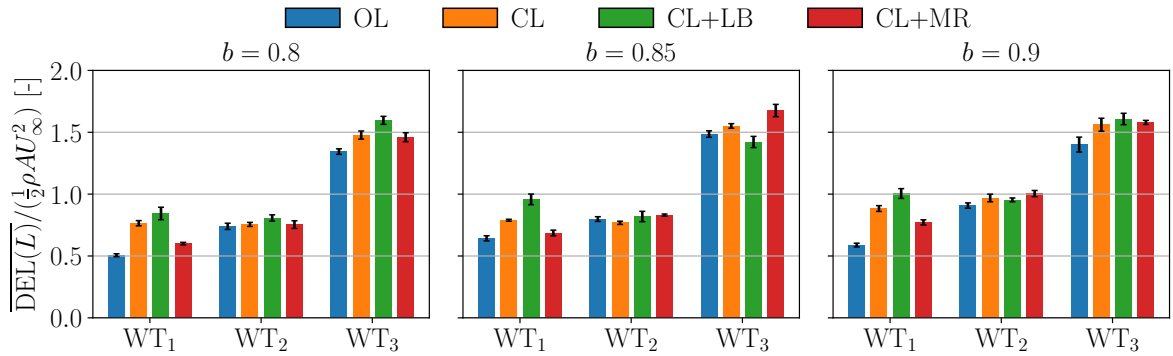


**Figure 20.** Normalized tower-base fore-aft DELs from the static turntable experiment for a wind direction  $\psi = 2.8^\circ$ , corresponding to 75% rotor overlap. Whiskers indicate the mean DEL over six repetitions and its uncertainty considering a 95% confidence level. Results are presented for three power-demand levels  $b$ .

Results show that waked turbines generally suffer more damage than those operating in freestream conditions, with WT<sub>3</sub> being consistently the most damaged. This is likely due to the highly turbulent local inflow and the partial wake impingement that introduce numerous load cycles on these machines. OL generally presents a rather low level of fatigue, which is due to the limited pitch actuation deriving from the lack of a closed-loop correction. At the same time, CL+LB yields the highest damage for WT<sub>1</sub>. In contrast to OL, this is caused by the more frequent blade pitch actuation that follows the occurrence of saturation events happening downstream. CL+MR reduces the fatigue of WT<sub>3</sub> in almost all instances, because wake steering applied to WT<sub>2</sub> mitigates partial wake overlap effects. CL+MR also reduces the fatigue of WT<sub>1</sub>, likely because fewer saturation events occur at downstream rotors, which WT<sub>1</sub> would otherwise have to compensate for through additional blade pitch activity. The analysis of blade pitch actuator duty cycle is reported in Appendix B.

465 Overall, the results shown here are consistent with the numerical findings by Tamaro et al. (2025b), but they differ from those reported by Vali et al. (2019), who observed significant fatigue reductions for downstream rotors when applying a load-balancing APC strategy. One possible explanation for this discrepancy is the substantially larger wind farm considered by Vali et al. (2019). A larger array facilitates spatial averaging of power and load fluctuations across multiple turbines, which may enhance the effectiveness of CL+LB. In contrast, the present study considers a limited number of turbines, where farm-level averaging effects are inherently reduced. While this difference may influence the achievable fatigue mitigation, particularly for downstream machines that are generally more prone to saturations, the analysis of small clusters appears to be less forgiving and hence can more clearly highlight the effects of difficult situations on tracking performance.

## 6 Dynamic wind direction experiments

The time series of the experiments conducted while moving the turntable are shown in Fig. 21 for the power requests  $b = 0.8$ ,  
475  $b = 0.85$ , and  $b = 0.9$ . In the plots, the expected available wind farm power  $P_{\text{greedy}}$  is displayed in grey in the background.  
 $P_{\text{greedy}}$  has been obtained with the turbines operating in greedy mode and fully aligned with the inflow, as discussed in Sect. 3.2.

From a first qualitative impression, all methods seem to follow the reference signal accurately. It is clear that OL and CL  
share the same power share setpoints  $\alpha_i$ , since  $P_{D,1}$ ,  $P_{D,2}$  and  $P_{D,3}$  are similar. In CL, however, some saturations can be seen,  
for instance when  $t \approx 100$  s and  $b = 0.9$ . CL+LB presents a very different distribution of power shares, and it appears that the  
480 individual power outputs  $P_{D,i}$  of the three turbines are often similar, possibly to balance the loads in conditions of low wake  
impingement. The power share distribution of CL+MR resembles that of OL, although  $P_{D,1}$  is generally lower and  $P_{D,3}$  higher  
due to wake steering.

Overall, the plots clearly show that, as the power demand is increased, the power request  $P_{\text{ref}}$  approaches the greedy power,  
and more saturation events arise, as indicated by the flat lines of  $P_{D,i}$  in CL, CL+LB, and CL+MR.

485 In the zoomed windows of the plot, an example is highlighted where OL presents a significant deviation from  $P_{\text{ref}}$  at the wind  
farm level, because of a saturation of WT<sub>2</sub> lasting approximately 10 seconds. This same problem also occurs for CL. However,  
the wind farm tracking error is clearly reduced because WT<sub>1</sub> and WT<sub>3</sub> are able to compensate. Quite differently, CL+LB and  
CL+MR show excellent tracking performance in the same scenario. This similar performance is, however, achieved in different  
ways: in CL+LB, both WT<sub>2</sub> and WT<sub>3</sub> are saturated and therefore operate in greedy mode, while WT<sub>1</sub> is fully responsible for  
490 tracking  $P_{\text{ref}}$ . In CL+MR, no saturation events are visible, which indicates generally larger power reserves for all turbines.

To present a more complete picture of the performance of the various algorithms, Appendix D reports additional zoomed  
segments of the plots shown in Fig. 21.

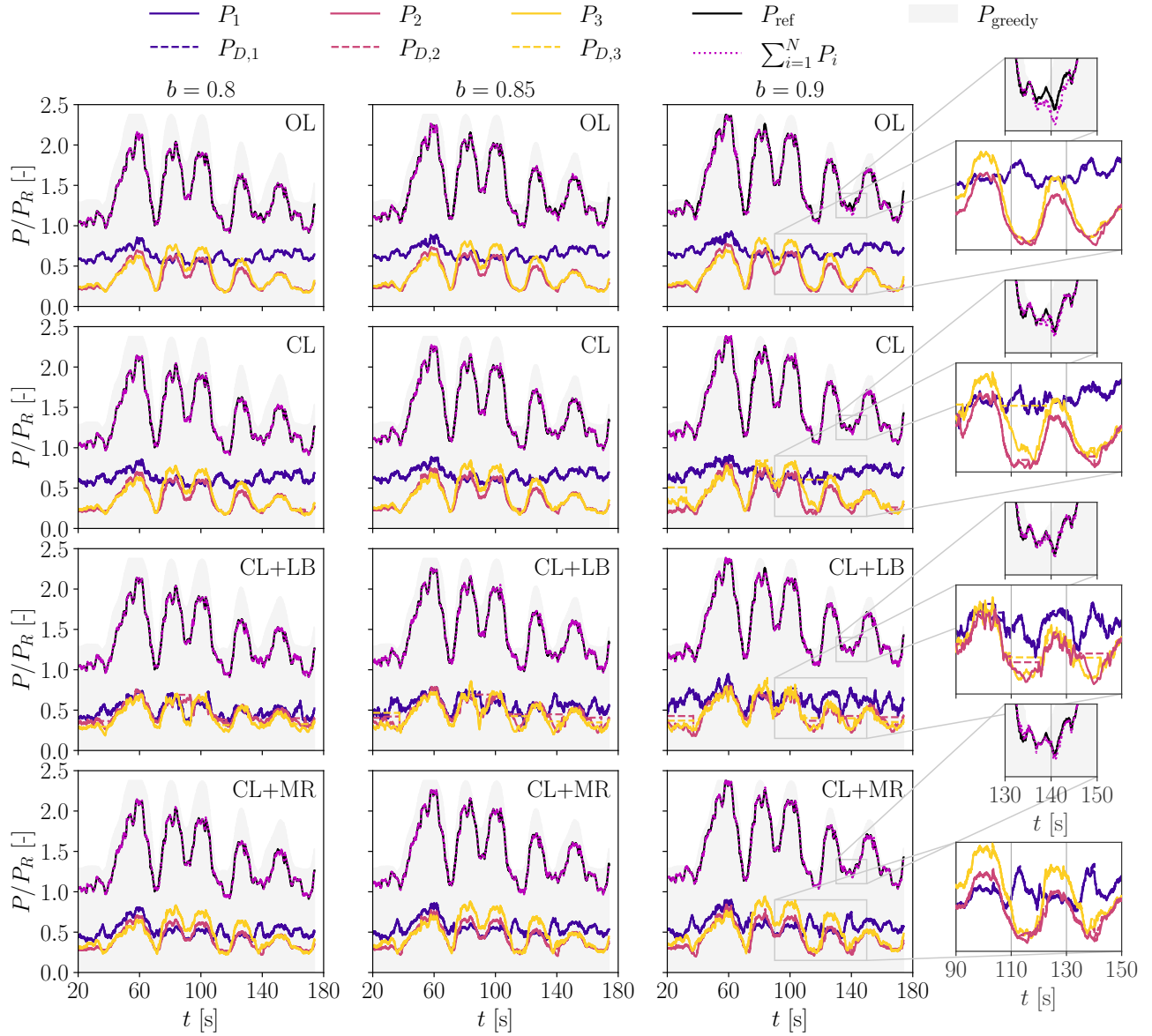
### 6.1 Power tracking accuracy

The RMS of the tracking error is shown in Fig. 22.

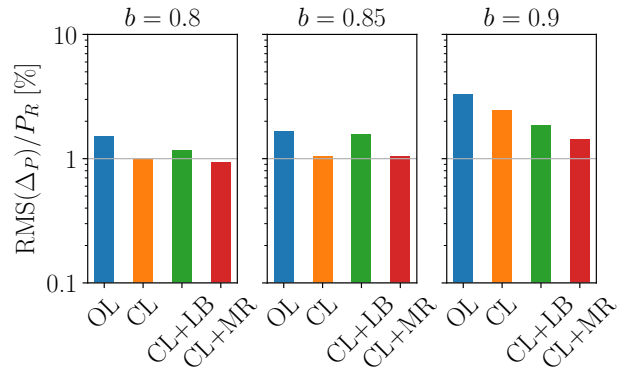
495 Consistently with the static wind direction results, OL shows the worst performance of all APC methods. At moderate power  
demands, for  $b \leq 0.85$ , CL and CL+MR exhibit the best performance. For  $b = 0.9$ , CL+MR provides the lowest RMS  $\Delta_P$ . The  
relative improvements achieved by CL+MR are less pronounced in the dynamic tests than in the static ones, as the effects of  
wake steering are less beneficial at large turntable misalignments where wake interactions are much reduced.

Figure 23 shows how the errors are distributed across the three turbines. It is important to mention that saturated turbines  
500 will display extreme error values  $\Delta_{P,i}$ , although this does not necessarily imply a large wind farm tracking error  $\Delta_P$ , since  
(except than for OL) non-saturated rotors can compensate for their error.

The figure shows relatively large tracking errors for OL, because of a lack of feedback capable of handling saturation  
conditions. Significant tracking errors can be observed for waked rotors in the case CL+LB, indicating persistent saturations,  
as seen in the zoomed regions of Fig. 21.



**Figure 21.** Time series of a power tracking experiment with dynamic wind direction variation, for the four APC algorithms and three power-demand levels  $b$ . The expected available wind farm power in greedy mode – based on the instantaneous wind direction – is shown in the background in grey.



**Figure 22.** RMS of power tracking errors for the four APC algorithms and three power-demand levels  $b$ . Experiment with dynamic wind direction variations.

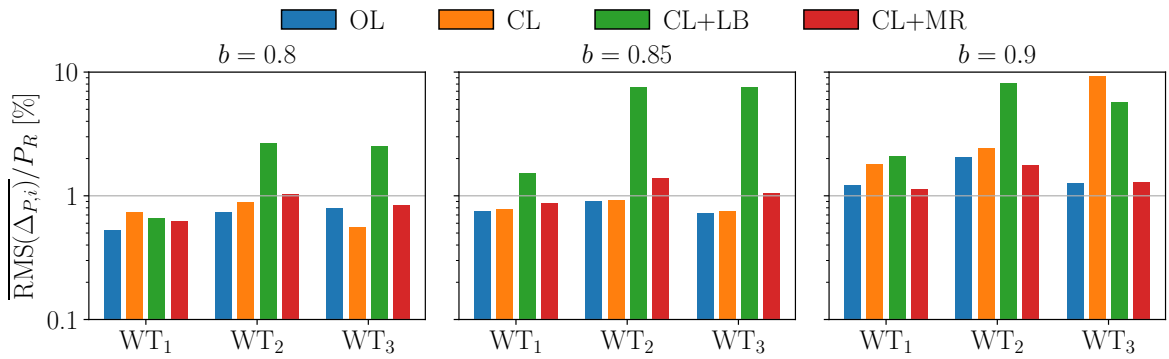


**Figure 23.** Local RMS of power tracking errors for the four APC algorithms and three power-demand levels  $b$ . Experiment with dynamic wind direction variations.

505 Figure 24 supports this analysis by presenting the mean collective blade pitch angles of the turbines during the experiment. As mentioned in the static direction study,  $\bar{\theta}_i$  can be seen as an indirect measure of the power reserve for the  $i$ th turbine.

Results show that CL+LB presents a significantly unbalanced power reserve distribution, shifted towards the upstream rotor, possibly as a result of the CLD loop. This is in agreement with the other quantities presented and discussed earlier in this section. As expected, CL+MR presents a rather large power reserve for all rotors, especially for WT<sub>3</sub>, thanks to wake steering,  
 510 but also for WT<sub>1</sub>, which is remarkable since this upstream turbine is often misaligned.

## 6.2 Loads and fatigue

Figure 25 presents the mean load-balancing error for the dynamic turntable experiment.

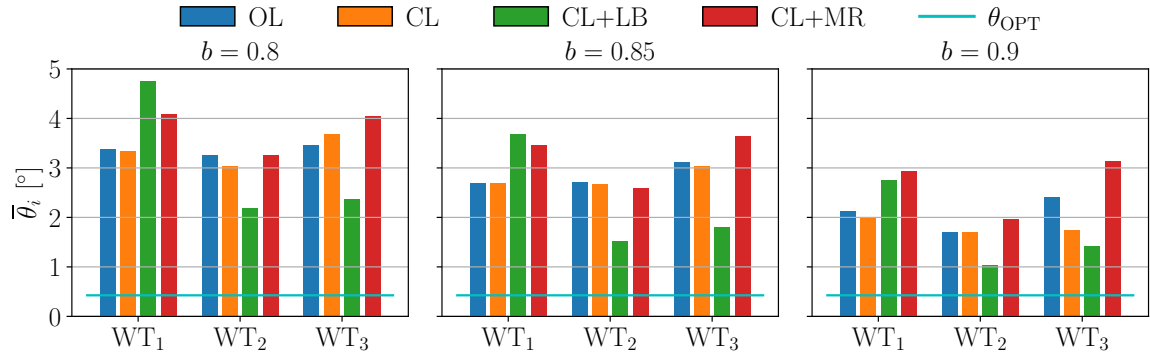


**Figure 24.** Mean collective blade pitch angle  $\bar{\theta}$  for the four APC algorithms and three power-demand levels  $b$ . Experiment with dynamic wind direction variations.

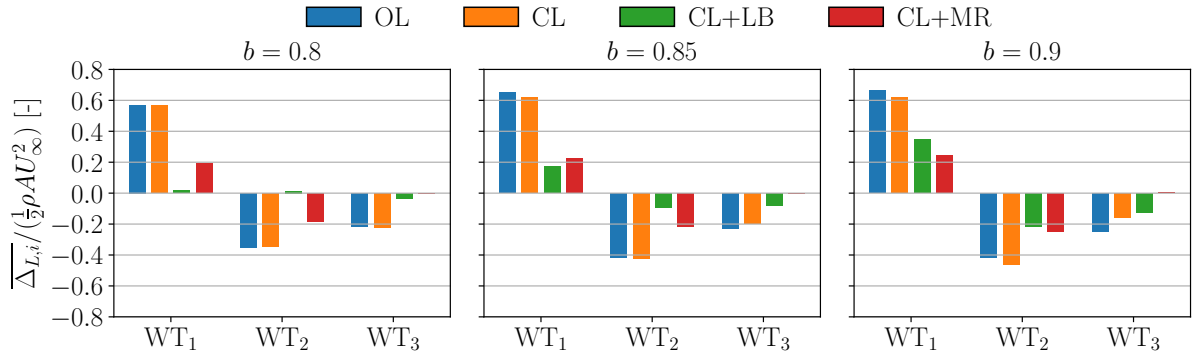


**Figure 25.** Mean local load-balancing error for tower-base fore-aft bending for the four APC algorithms and three power-demand levels  $b$ . The error is normalized by  $\frac{1}{2} \rho U_{\infty}^2$ . Positive values indicate loading above the wind farm average. Experiment with dynamic wind direction variations.

For OL and CL, the front turbine  $WT_1$  exhibits the highest loading, which progressively diminishes for rotors located further downstream. As seen already in the static cases, CL+LB effectively balances the loads. Its effectiveness is excellent at  $b = 0.8$  but – importantly – gradually deteriorates as  $b$  increases since more saturation events arise that modify the power share distribution to prioritize tracking accuracy. CL+MR displays the second-best performance for the lower  $b$  values, but ultimately outperforms CL+LB for  $b = 0.9$ . This shows the importance of controlling saturations, and the limits of a purely load-balancing strategy.

Figure 26 reports the normalized tower-base fore-aft DELs.

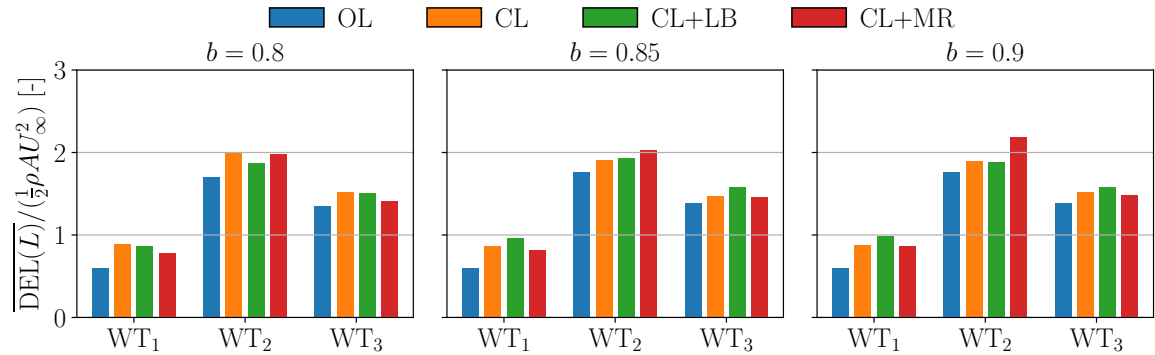


**Figure 26.** Tower-base fore-aft DELs for the four APC algorithms and three power-demand levels  $b$ . DELs are normalized by  $\frac{1}{2}\rho U_\infty^2$ . Experiment with dynamic wind direction variations.

520 These results generally indicate a higher fatigue for  $WT_2$ , followed by  $WT_3$  and  $WT_1$ , which is the least affected turbine.  $WT_2$  is also the rotor that generally has the smallest power margin in the farm, as shown in Fig. 24. This result is consistent with the findings of Tamaro et al. (2025b), which showed that fatigue is driven by the low-frequency load cycles that occur because of saturation events. OL generally exhibits the lowest fatigue, due to the smoother control of the rotors. The proposed CL+MR method reduces  $\overline{\text{DEL}(L)}$  for  $WT_1$  and  $WT_3$  compared to other methods featuring a closed loop, while it increases it

525 for  $WT_2$ , possibly due to a lower power margin deriving from the  $\alpha_i$  and  $\gamma_i$  LUTs.

## 7 Conclusions

A maximum-reserve approach for robust wind farm power tracking that combines wake steering and induction control has been tested experimentally in a wind tunnel. The objective of the algorithm is to enhance power reserves across the wind farm to mitigate the effects of wind lulls, thereby generating a more accurate tracking of the desired power signal.

530 To support the experimental work, a steady-state model was developed, based on a modified version of FLORIS. This model accounts for the aerodynamic interactions resulting from simultaneous yaw misalignment and curtailed operation, as well as specific wind tunnel inflow characteristics and chord-based Reynolds number effects caused by the small scale of the turbines.

The experiments were conducted in a large boundary-layer wind tunnel using a small cluster of three scaled rotors with minimal blockage. The first set of experiments considered two wind farm layouts to replicate varying levels of wake impingement. 535 A second, unprecedented set of APC experiments involved dynamically varying the wind direction using a large turntable.

The maximum-reserve method was compared with three alternative APC algorithms sourced from the recent literature. All controllers were implemented on a dedicated cabinet, enabling real-time communication to and from the controllers running on the individual turbines. The performance of the various controllers was evaluated in terms of power tracking accuracy, power reserves, structural loads, and fatigue.

540 The main findings of this study are as follows:

- A steady-state analysis confirms that wake impingement reduces power reserves of downstream rotors. The combined use of wake steering and induction control effectively enhances local power reserves, thereby improving overall power tracking accuracy.
- The treatment of saturation conditions significantly affects power tracking performance. The open-loop algorithm showed 545 the poorest performance in most cases. However, introducing a simple feedback loop and a compensation strategy for saturated rotors led to substantial improvements.
- Results from the dynamic wind direction experiments corroborated the findings from the fixed-direction runs, highlighting the strong potential of wake control in APC applications.
- Dispatching power setpoints to balance loads proved effective in reducing fatigue compared to both open-loop and 550 closed-loop controllers with fixed setpoints. However, load-balancing setpoints may lead to localized saturation, particularly at high power-demand levels, which in turn negatively affects loading.

Future work may extend this study by investigating the role of curtailment strategies on power tracking performance. Another area of investigation that should be pursued is the direct inclusion of loads in the maximum-reserve formulation because, as seen here, a correct management of reserves can have major implications on loading.

## 555 Appendix A: Floris wake parameters

Tables A1, A2 and A3 present the values of the parameters of the wake deflection, turbulence, and wake deficit models, respectively.

**Table A1.** Values of the parameters of the deflection model (Bastankhah and Porté-Agel, 2014).

$\alpha_d$	$b_d$	$A$	$B$	$k_a$	$k_b$	$d_m$	$\epsilon_{gain}$
0	0	0.58	0.077	0.38	0.004	1	0.2

**Table A2.** Values of the parameters of the turbulence model (Crespo and Hernández, 1996).

Initial	Constant	$a_i$	Downstream
0.1057	0.3401	0.9558	-0.3562

**Table A3.** Values of the parameters of the Gauss deficit model (Bastankhah and Porté-Agel, 2014).

$A$	$\beta$	$k_a$	$k_b$
0.8647	0.1226	0.4783	0.0044

## Appendix B: Blade pitch actuator duty cycle

The actuator duty cycle (ADC) of blade pitch is shown for the static turntable experiments in Figs. B1 and B2 for  $\psi = 2.8^\circ$  and  $\psi = 5.7^\circ$ , respectively. ADC for the blade pitch angle  $\theta$  is defined as (Bottasso et al., 2013)

$$\text{ADC}_\theta = \frac{1}{T} \int_0^T \frac{\dot{\theta}(t)}{\dot{\theta}_{\max}} dt, \quad (\text{B1})$$

where  $\dot{\theta}$  is the pitch rate.

Results appear to be strongly dependent on the power-demand level  $b$ . When  $b = 0.8$ , waked turbines show a higher pitch activity than the upstream turbine  $\text{WT}_1$ . This condition persists for OL and CL+MR in most of the other  $b$  scenarios and for both wind directions  $\psi$ . For CL and CL+MR, on the contrary, for  $b = 0.9$  it is the front turbine  $\text{WT}_1$  that displays the highest pitch activity, most likely due to the need for compensating the saturation events happening at the downstream waked turbines. It should also be noted that when a turbine saturates, its pitch lies at  $\theta = \theta_{\text{OPT}}$  until the saturation criteria are not met anymore, and this automatically reduces ADC.

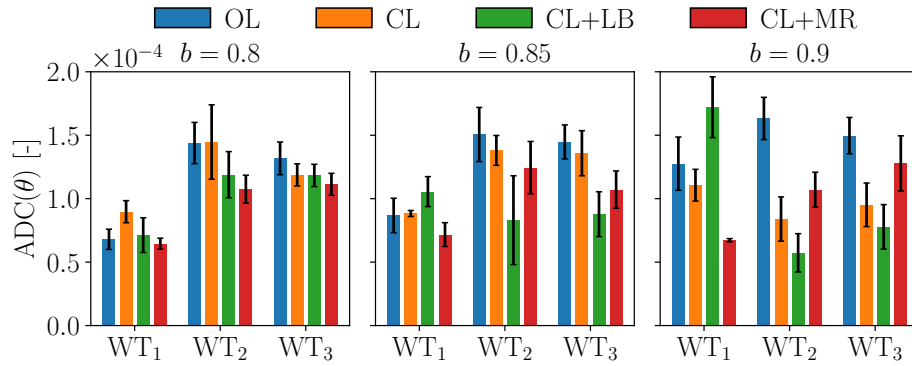


**Figure B1.** Blade pitch ADC for the static turntable experiment with wind direction  $\psi = 2.8^\circ$ , corresponding to 75% rotor overlap. Whiskers indicate 95% confidence intervals. Results are presented for three power-demand requests  $b$ .

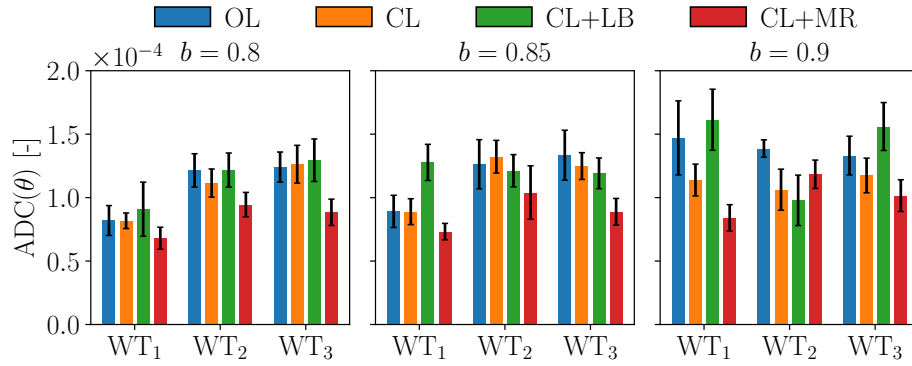


**Figure B2.** Blade pitch ADC for the static turntable experiment with wind direction  $\psi = 5.7^\circ$ , corresponding to 50% rotor overlap. Whiskers indicate 95% confidence intervals. Results are presented for three power-demand requests  $b$ .

## Appendix C: Load-balancing error

570 For completeness, Fig. C1 reports the mean local load-balancing error for the case  $\psi = 5.7^\circ$  (50% rotor overlap). The case  $\psi = 5.7^\circ$  (75% rotor overlap) was shown earlier in Fig. 19.

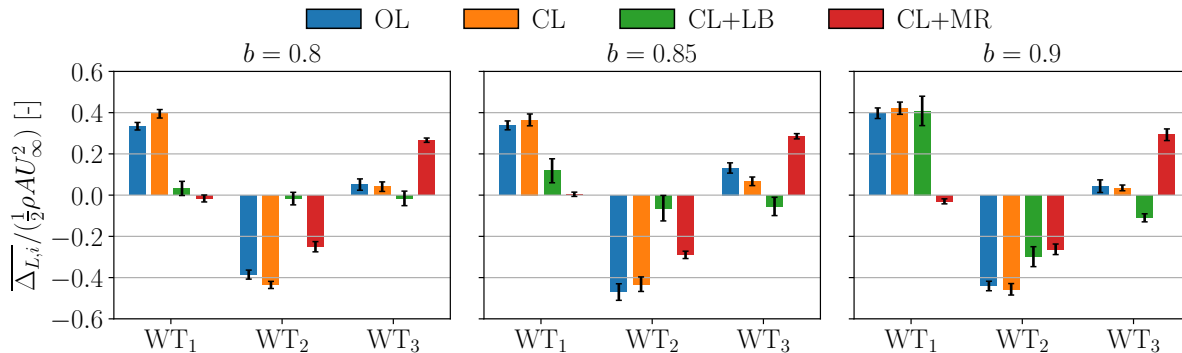


**Figure C1.** Mean local load-balancing error for the tower-base fore-aft bending moment for the static turntable experiment with wind direction  $\psi = 5.7^\circ$ , corresponding to 75% rotor overlap.  $L$  is normalized with  $\frac{1}{2}\rho U_\infty^2$ . Positive values indicate loading above the wind farm average. Results are presented for three power-demand requests  $b$ .

## Appendix D: Zoomed segments of Fig. 21 (power tracking time series under dynamic wind direction conditions)

This appendix reports zoomed segments of the power tracking time series shown in Fig. 21, which were obtained under dynamic wind direction conditions.

575 Figure D1 presents the first 20 seconds of the experiment for a low average power-demand level  $b = 0.8$ . The plots highlight the similar power share distributions of OL and CL. OL presents a slight deviation from  $P_{\text{ref}}$  at  $t = 10$  s, which is improved in CL thanks to the closed-loop correction that it implements. Figure D1c shows that the power share distribution is equal among the rotors for CL+LB. Although a saturation of WT<sub>2</sub> occurs at  $t = 10$  s, it does not affect the power tracking accuracy, because WT<sub>1</sub> and WT<sub>3</sub> adjust their power demand to compensate. Finally, Fig. D1d shows that the power share distribution generated  
 580 by CL+MR is significantly different from the other cases, with WT<sub>3</sub> producing the most power as a result of the wake steering performed by the upstream turbines. The power outputs of the turbines also appear to be much smoother than in the other cases.

Next, Fig. D2 presents 8 seconds from experiments conducted with a larger average power-demand level equal to  $b = 0.85$ . Figure D2a clearly shows the difficulty of the OL controller in tracking  $P_{\text{ref}}$  at  $t = 60$  s. In particular,  $P_1$  exhibits significant deviations from  $P_{D,1}$ . The figure shows also that CL and CL+MR are able to improve the power tracking accuracy; however,  
 585 even in these cases, WT<sub>1</sub> struggles to follow its demand, leading to saturations – for instance at  $t = 62$  s. In CL+LB, the load-balancing loop tends to equalize the power shares, but this results in a reduced power reserve for WT<sub>2</sub>, which in fact saturates at  $t = 62$  s.

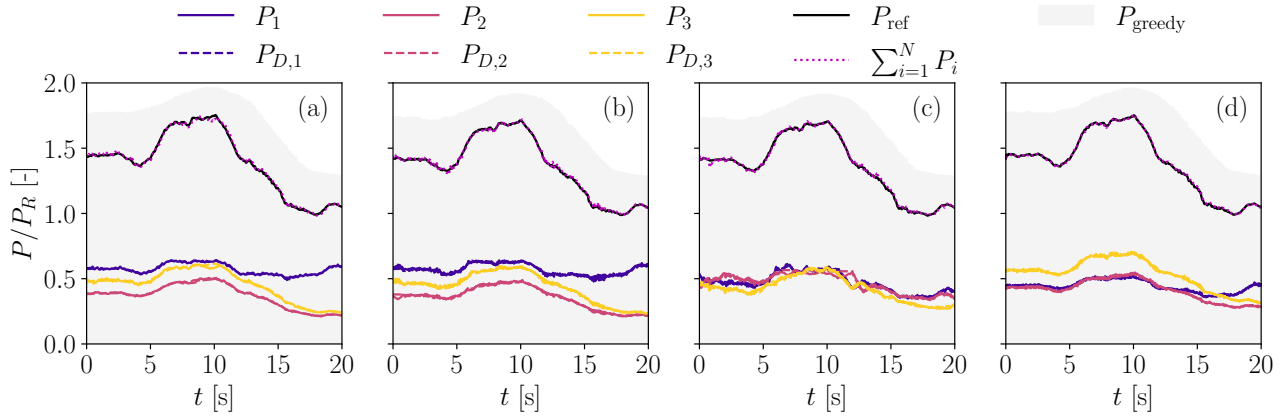


**Figure D1.** Enlarged segment of time series of a power tracking experiment with dynamic wind direction variation for a power-demand level  $b = 0.8$ . The wind farm control strategies are OL (a), CL (b), CL+LB (c), and CL+MR (d). The expected available wind farm power in greedy mode – based on the instantaneous wind direction – is shown in the background in grey.

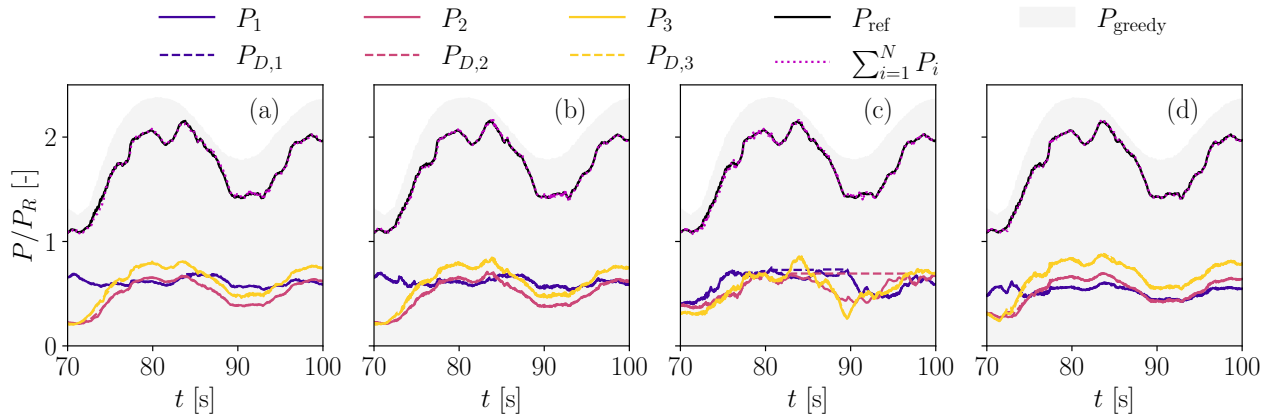


**Figure D2.** Enlarged segment of time series of a power tracking experiment with dynamic wind direction variation, for a power-demand level  $b = 0.85$ . The wind farm control strategies are OL (a), CL (b), CL+LB (c), and CL+MR (d). The expected available wind farm power in greedy mode – based on the instantaneous wind direction – is shown in the background in grey.

Finally, Fig. D3 focuses on 20 seconds towards the end of the experiments for a high average power-demand level  $b = 0.9$ . The plots clearly show that both OL and CL exhibit critical tracking errors at  $t = 164$  s, with  $WT_2$  being responsible for the error in both cases. In CL, this leads to its saturation. It is also clearly visible that, as  $P_{D,1}$  is increased due to the saturation of  $WT_2$ ,  $WT_1$  saturates as well. Figure D3c shows that the load-balancing algorithm attempts to increase the power share of  $WT_2$  and  $WT_3$  at  $t = 155$  s. However, this is incompatible with their local power reserves and results in the saturation of both rotors for  $t > 160$  s. Nevertheless, the local power-tracking errors of  $WT_2$  and  $WT_3$  are redistributed to  $WT_1$ , which is able to ensure good tracking of  $P_{\text{ref}}$ . For CL+MR, the turbine power outputs are smoother and free from saturations.

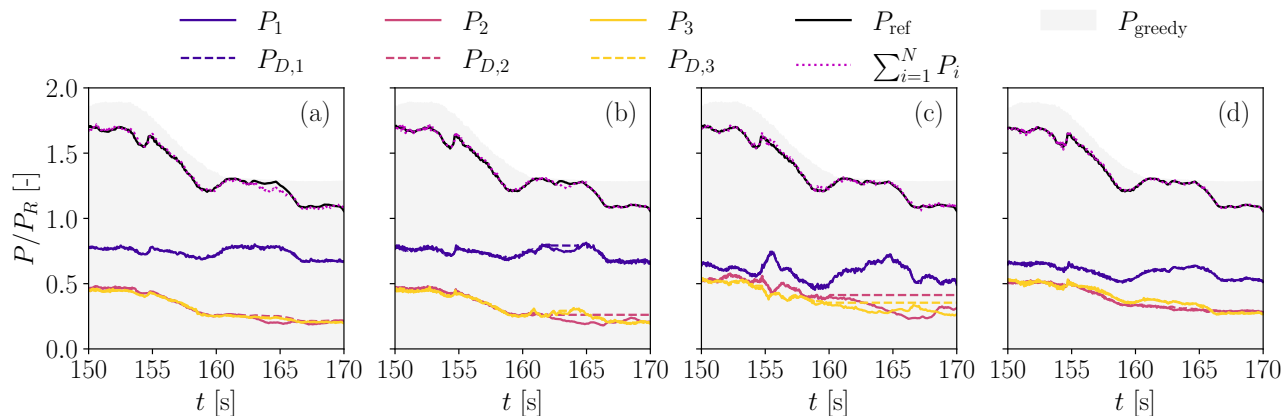


**Figure D3.** Enlarged segment of time series of a power tracking experiment with dynamic wind direction variation, for a power-demand level  $b = 0.9$ . The wind farm control strategies are OL **(a)**, CL **(b)**, CL+LB **(c)**, and CL+MR **(d)**. The expected available wind farm power in greedy mode – based on the instantaneous wind direction – is shown in the background in grey.

595 **Appendix E: Nomenclature**

	<b>A</b>	Ambient conditions
	$b$	Shift of normalized power-demand signal (i.e. average power-demand level)
	$C_P$	Power coefficient
	$C_T$	Thrust coefficient
600	$c$	Amplitude of normalized power-demand signal
	$D$	Rotor diameter
	$K^I$	Control gain (integral)
	$K^P$	Control gain (proportional)
	$L$	Tower base fore-aft bending moment
605	$m$	Power reserve
	$N$	Total number of wind turbines
	$n_k^{\text{AGC}}$	Normalized power-demand signal
	$P$	Wind turbine power
	$P_D$	Wind turbine power demand
610	$P_R$	Rated power
	$P_{\text{ref}}$	Reference power signal
	$P_{\text{ref}}^{\text{PI}}$	Closed-loop, APC control output
	$R$	Rotor radius
	$S$	Number of saturated rotors
615	$t$	Time
	$U$	Rotor-equivalent wind speed
	$U_\infty$	Freestream wind speed measured at hub height
	<b>u</b>	Control inputs
620	$\alpha$	Power-share setpoint
	$\gamma$	Misalignment angle
	$\Delta_L$	Load-balancing error
	$\Delta_P$	Power tracking error
	$\epsilon$	Auxiliary power scaling factor
625	$\eta_P$	Power loss factor
	$\theta$	Blade pitch angle
	$\lambda$	Tip speed ratio
	$\rho$	Air density

	$\tau$	Time instant index
630	$\psi$	Wind direction
	$\Omega$	Rotor angular speed
	$\Omega_R$	Rated rotor angular speed
	AGC	Automatic generation control
635	APC	Active power control
	CL	Closed loop
	CLD	Coordinated load distribution
	CL+LB	Closed loop with load balancing
	CL+MR	Closed loop with maximum reserve
640	DEL	Damage equivalent load
	LUT	Look-up table
	FLORIS	FLOW Redirection and Induction in Steady State
	OL	Open loop
	PI	Proportional – integral
645	RMS	Root mean square
	TI	Turbulence intensity
	TSO	Transmission system operator
	WF	Wind farm
	WT	Wind turbine
650		

*Code and data availability.* The Simulink models of the APC controllers, and the C++ codes generated from them are accessible in the European open repository Zenodo at <https://doi.org/10.5281/zenodo.17551525> (Tamaro et al., 2025a). A video of one of the experiments is available at <https://youtu.be/ClfaI2VKz2g>.

*Author contributions.* CLB developed the formulation of the maximum-reserve APC method and supervised the overall research. ST implemented the model, performed the experiments, and conducted the steady state analyses with FLORIS. FC coordinated the experimental campaign and supported the development and implementation of the controllers. DB and FM contributed to the wind tunnel campaign. All authors contributed to the interpretation of the results. CLB and ST wrote the paper, with contributions by FC. All authors provided important input to this research work through discussions and feedback, and improved the manuscript.

*Competing interests.* At least one of the (co-)authors is a member of the editorial board of *Wind Energy Science*.

660 *Financial support.* This work has been supported in part by the PowerTracker project, which receives funding from the German Federal Ministry for Economic Affairs and Climate Action (FKZ: 03EE2036A). This work has also been partially supported by the SUDOCO project, which receives funding from the European Union's Horizon Europe Programme under grant agreement 101122256.

*Acknowledgements.* The authors express their gratitude to the wind tunnel team at Politecnico di Milano for providing assistance in the experiments.

## 665 References

- Aho, J., Buckspan, A., Laks, J., Fleming, P., Jeong, Y., Dunne, F., Churchfield, M., Pao, L., and Johnson, K.: A tutorial of wind turbine control for supporting grid frequency through active power control, in: 2012 American Control Conference (ACC), pp. 3120–3131, <https://doi.org/10.1109/ACC.2012.6315180>, 2012.
- Bachmann electronic GmbH: System overview, Bachmann electronic GmbH, Feldkirch, 2017.
- 670 Bastankhah, M. and Porté-Agel, F.: A new analytical model for wind-turbine wakes, *Renewable Energy*, 70, 116–123, <https://doi.org/https://doi.org/10.1016/j.renene.2014.01.002>, special issue on aerodynamics of offshore wind energy systems and wakes, 2014.
- Boersma, S., Rostampour, V., Doekemeijer, B., van Geest, W., and van Wingerden, J.-W.: A constrained model predictive wind farm controller providing active power control: an LES study, *Journal of Physics: Conference Series*, 1037, 032023, <https://doi.org/10.1088/1742-6756/1037/3/032023>, 2018.
- 675 Bortolotti, P., Tarres, H. C., Dykes, K. L., Merz, K., Sethuraman, L., Verelst, D., and Zahle, F.: IEA Wind TCP Task 37: Systems Engineering in Wind Energy - WP2.1 Reference Wind Turbines, Tech. rep., National Renewable Energy Lab. (NREL), <https://doi.org/10.2172/1529216>, 2019.
- Bossanyi, E. and Ruisi, R.: Axial induction controller field test at Sedini wind farm, *Wind Energy Science*, 6, 389–408, <https://doi.org/10.5194/wes-6-389-2021>, 2021.
- 680 Bottasso, C., Campagnolo, F., Croce, A., and Tibaldi, C.: Optimization-based study of bend–twist coupled rotor blades for passive and integrated passive/active load alleviation, *Wind Energy*, 16, 1149–1166, <https://doi.org/https://doi.org/10.1002/we.1543>, 2013.
- Bottasso, C. L. and Campagnolo, F.: Wind tunnel testing of wind turbines and farms, in: *Handbook of Wind Energy Aerodynamics*, edited by Stoevesandt, B., Schepers, G., Fuglsang, P., and Sun, Y., pp. 1077–1126, Springer International Publishing, Cham, ISBN 978-3-030-31307-4, [https://doi.org/10.1007/978-3-030-31307-4\\_54](https://doi.org/10.1007/978-3-030-31307-4_54), 2022.
- 685 Bottasso, C. L., Campagnolo, F., and Petrović, V.: Wind tunnel testing of scaled wind turbine models: Beyond aerodynamics, *J. Wind Eng. Ind. Aerodyn*, 127, 2014.
- Boyle, J. and Littler, T.: A review of frequency-control techniques for wind power stations to enable higher penetration of renewables onto the Irish power system, *Energy Reports*, 12, 5567–5581, <https://doi.org/https://doi.org/10.1016/j.egy.2024.11.031>, 2024.
- 690 Brayton, R., Director, S., Hachtel, G., and Vidigal, L.: A new algorithm for statistical circuit design based on quasi-Newton methods and function splitting, *IEEE Transactions on Circuits and Systems*, 26, 784–794, <https://doi.org/10.1109/TCS.1979.1084701>, 1979.
- Bromm, M., Rott, A., Beck, H., Vollmer, L., Steinfeld, G., and Kühn, M.: Field investigation on the influence of yaw misalignment on the propagation of wind turbine wakes, *Wind Energy*, 21, 1011–1028, <https://doi.org/https://doi.org/10.1002/we.2210>, 2018.
- Campagnolo, F., Petrović, V., Schreiber, J., Nanos, E. M., Croce, A., and Bottasso, C. L.: Wind tunnel testing of a closed-loop wake deflection controller for wind farm power maximization, *Journal of Physics: Conference Series*, 753, 032006, <https://doi.org/10.1088/1742-6596/753/3/032006>, 2016.
- 695 Campagnolo, F., Weber, R., Schreiber, J., and Bottasso, C. L.: Wind tunnel testing of wake steering with dynamic wind direction changes, *Wind Energy Science*, 5, 1273–1295, <https://doi.org/10.5194/wes-5-1273-2020>, 2020.
- Campagnolo, F., Castellani, F., Natili, F., Astolfi, D., and Mühle, F.: Wind tunnel testing of yaw by individual pitch control applied to wake steering, *Frontiers in Energy Research*, 10, <https://doi.org/10.3389/fenrg.2022.883889>, 2022a.
- 700

- Campagnolo, F., Imširović, L., von Braunbehrens, R., and Bottasso, C. L.: Further calibration and validation of FLORIS with wind tunnel data, *Journal of Physics: Conference Series*, 2265, 022 019, <https://doi.org/10.1088/1742-6596/2265/2/022019>, 2022b.
- Canet, H., Bortolotti, P., and Bottasso, C.: On the scaling of wind turbine rotors, *Wind Energy Science*, 6, 601–626, <https://doi.org/10.5194/wes-6-601-2021>, 2021.
- 705 Cossu, C.: Wake redirection at higher axial induction, *Wind Energy Science*, 6, 377–388, <https://doi.org/10.5194/wes-6-377-2021>, 2021.
- Crespo, A. and Hernández, J.: Turbulence characteristics in wind-turbine wakes, *Journal of Wind Engineering and Industrial Aerodynamics*, 61, 71–85, [https://doi.org/https://doi.org/10.1016/0167-6105\(95\)00033-X](https://doi.org/https://doi.org/10.1016/0167-6105(95)00033-X), 1996.
- Doekemeijer, B. M., Kern, S., Maturu, S., Kanev, S., Salbert, B., Schreiber, J., Campagnolo, F., Bottasso, C. L., Schuler, S., Wilts, F., Neumann, T., Potenza, G., Calabretta, F., Fioretti, F., and van Wingerden, J.-W.: Field experiment for open-loop yaw-based wake steering at a commercial onshore wind farm in Italy, *Wind Energy Science*, 6, 159–176, <https://doi.org/10.5194/wes-6-159-2021>, 2021.
- 710 Ela, E., Gevorgian, V., Fleming, P., Zhang, Y. C., Singh, M., Muljadi, E., Scholbrook, A., Aho, J., Buckspan, A., Pao, L., Singhvi, V., Tuohy, A., Pourbeik, P., Brooks, D., and Bhatt, N.: Active power controls from wind power: bridging the gaps, Tech. Rep. NREL/TP-5D00-60574, National Renewable Energy Lab. (NREL), <https://doi.org/10.2172/1117060>, 2014.
- Fleming, P., Aho, J., Gebraad, P., Pao, L., and Zhang, Y.: Computational fluid dynamics simulation study of active power control in wind plants, in: 2016 American Control Conference (ACC), pp. 1413–1420, <https://doi.org/10.1109/ACC.2016.7525115>, 2016.
- 715 Fleming, P., King, J., Dykes, K., Simley, E., Roadman, J., Scholbrock, A., Murphy, P., Lundquist, J. K., Moriarty, P., Fleming, K., van Dam, J., Bay, C., Mudafort, R., Lopez, H., Skopek, J., Scott, M., Ryan, B., Guernsey, C., and Brake, D.: Initial results from a field campaign of wake steering applied at a commercial wind farm – Part 1, *Wind Energy Science*, 4, 273–285, <https://doi.org/10.5194/wes-4-273-2019>, 2019.
- 720 Frederik, J. A., Doekemeijer, B. M., Mulders, S. P., and van Wingerden, J.-W.: The helix approach: using dynamic individual pitch control to enhance wake mixing in wind farms, *Wind Energy*, 23, 1739–1751, <https://doi.org/https://doi.org/10.1002/we.2513>, 2020a.
- Frederik, J. A., Weber, R., Cacciola, S., Campagnolo, F., Croce, A., Bottasso, C., and van Wingerden, J.-W.: Periodic dynamic induction control of wind farms: proving the potential in simulations and wind tunnel experiments, *Wind Energy Science*, 5, 245–257, <https://doi.org/10.5194/wes-5-245-2020>, 2020b.
- 725 Gonzalez Silva, J., Doekemeijer, B. M., Ferrari, R., and van Wingerden, J.-W.: Active power control of wind farms: an instantaneous approach on waked conditions, *Journal of Physics: Conference Series*, 2265, 022 056, <https://doi.org/10.1088/1742-6596/2265/2/022056>, 2022.
- Gonzalez Silva, J., van der Hoek, D., Ferrari, R., and van Wingerden, J. W.: Wind tunnel testing of wind turbine and wind farm control strategies for active power regulation, *Journal of Renewable and Sustainable Energy*, 16, 053 302, <https://doi.org/10.1063/5.0215493>, 2024.
- 730 Heck, K., Johlas, H., and Howland, M.: Modelling the induction, thrust and power of a yaw-misaligned actuator disk, *Journal of Fluid Mechanics*, 959, A9, <https://doi.org/10.1017/jfm.2023.129>, 2023.
- Howland, M. F., Lele, S. K., and Dabiri, J. O.: Wind farm power optimization through wake steering, *Proceedings of the National Academy of Sciences*, 116, 14 495–14 500, <https://doi.org/10.1073/pnas.1903680116>, 2019.
- Jensen, N.: A note on wind generator interaction, no. 2411 in *Risø-M*, Risø National Laboratory, ISBN 87-550-0971-9, 1983.
- 735 Jiménez, A., Crespo, A., and Migoya, E.: Application of a LES technique to characterize the wake deflection of a wind turbine in yaw, *Wind Energy*, 13, 559–572, <https://doi.org/https://doi.org/10.1002/we.380>, 2010.
- Jonkman, J., Butterfield, S., Musial, W., and Scott, G.: Definition of a 5-MW Reference Wind Turbine for Offshore System Development, Tech. rep., National Renewable Energy Laboratory, <https://doi.org/10.2172/947422>, 2009.

- Liew, J. and Larsen, G. C.: How does the quantity, resolution, and scaling of turbulence boxes affect aeroelastic simulation convergence?,  
740 *Journal of Physics: Conference Series*, 2265, 032 049, <https://doi.org/10.1088/1742-6596/2265/3/032049>, 2022.
- Lin, M. and Porté-Agel, F.: Wake meandering of wind turbines under dynamic yaw control and impacts on power and fatigue, *Renewable Energy*, 223, 120 003, <https://doi.org/https://doi.org/10.1016/j.renene.2024.120003>, 2024.
- Meyers, J., Bottasso, C. L., Dykes, K., Fleming, P., Gebraad, P., Giebel, G., Göçmen, T., and van Wingerden, J.-W.: Wind farm flow control: prospects and challenges, *Wind Energy Science Discussions*, <https://doi.org/https://doi.org/10.5194/wes-2022-24>, 2022.
- 745 Mühle, F. V., Heckmeier, F. M., Campagnolo, F., and Breitsamter, C.: Wind tunnel investigations of an individual pitch control strategy for wind farm power optimization, *Wind Energy Science*, 9, 1251–1271, <https://doi.org/10.5194/wes-9-1251-2024>, 2024.
- Munters, W. and Meyers, J.: Towards practical dynamic induction control of wind farms: analysis of optimally controlled wind-farm boundary layers and sinusoidal induction control of first-row turbines, *Wind Energy Science*, 3, 409–425, <https://doi.org/10.5194/wes-3-409-2018>, 2018.
- 750 Nanos, E. M., Bottasso, C. L., Tamaro, S., Manolas, D. I., and Riziotis, V. A.: Vertical wake deflection for floating wind turbines by differential ballast control, *Wind Energy Science*, 7, 1641–1660, <https://doi.org/10.5194/wes-7-1641-2022>, 2022.
- National Renewable Energy Laboratory: NREL/floris: v3.0, Zenodo, <https://doi.org/10.5281/zenodo.6320841>, 2022.
- Oudich, Y., Gyselink, J., De Belie, F., and Kinnaert, M.: Providing power reserve for secondary grid frequency regulation of offshore wind farms through yaw control, *Wind Energy*, 26, 850–873, <https://doi.org/https://doi.org/10.1002/we.2845>, 2023.
- 755 Petrović, V., Schottler, J., Neunaber, I., Hölling, M., and Kühn, M.: Wind tunnel validation of a closed loop active power control for wind farms, *Journal of Physics: Conference Series*, 1037, 032 020, <https://doi.org/10.1088/1742-6596/1037/3/032020>, 2018.
- Porté-Agel, F., Wu, Y.-T., and Chen, C.-H.: A numerical study of the effects of wind direction on turbine wakes and power losses in a large wind farm, *Energies*, 6, 5297–5313, <https://doi.org/10.3390/en6105297>, 2013.
- Profibus Nutzerorganisation e. V. (PNO): Profinet system – Description technology and application, Profibus & Profinet International (PI),  
760 Haid-und-Neu-Str. 7, 76131 Karlsruhe, Germany, 4 edn., 2018.
- Shapiro, C. R., Bauweraerts, P., Meyers, J., Meneveau, C., and Gayme, D. F.: Model-based receding horizon control of wind farms for secondary frequency regulation, *Wind Energy*, 20, 1261–1275, <https://doi.org/https://doi.org/10.1002/we.2093>, 2017.
- Starke, G. M., Meneveau, C., King, J., and Gayme, D. F.: Yaw-augmented control for wind farm power tracking, in: 2023 American Control Conference (ACC), pp. 184–191, <https://doi.org/10.23919/ACC55779.2023.10156444>, 2023.
- 765 Tamaro, S. and Bottasso, C. L.: A new wind farm active power control strategy to boost tracking margins in high-demand scenarios, in: 2023 American Control Conference (ACC), pp. 192–197, <https://doi.org/10.23919/ACC55779.2023.10156275>, 2023.
- Tamaro, S., Campagnolo, F., and Bottasso, C. L.: On the power and control of a misaligned rotor – Beyond the cosine law, *Wind Energy Science*, 9, 1547–1575, <https://doi.org/10.5194/wes-9-1547-2024>, 2024a.
- Tamaro, S., Guilloré, A., Anand, A., Mühle, F. V., Campagnolo, F., and Bottasso, C. L.: Validation of induction/steering reserve-boosting  
770 active power control by a wind tunnel experiment with dynamic wind direction changes, *Journal of Physics: Conference Series*, 2767, 092 067, <https://doi.org/10.1088/1742-6596/2767/9/092067>, 2024b.
- Tamaro, S., Bortolin, D., Campagnolo, F., Mühle, F. V., and Bottasso, C. L.: Scaled testing of maximum-reserve active power control, Zenodo [source code and data set], <https://doi.org/10.5281/zenodo.17551525>, 2025a.
- Tamaro, S., Campagnolo, F., and Bottasso, C. L.: A robust active power control algorithm to maximize wind farm power tracking margins in  
775 waked conditions, *Wind Energy Science*, 10, 2705–2728, <https://doi.org/10.5194/wes-10-2705-2025>, 2025b.
- The MathWorks, Inc.: MATLAB, Version 9.13.0 (R2022b), <https://www.mathworks.com>, computer software, 2022.

- Vali, M., Petrović, V., Steinfeld, G., Y. Pao, L., and Kühn, M.: An active power control approach for wake-induced load alleviation in a fully developed wind farm boundary layer, *Wind Energy Science*, 4, 139–161, <https://doi.org/10.5194/wes-4-139-2019>, 2019.
- van der Hoek, D., Kanev, S., Allin, J., Bieniek, D., and Mittelmeier, N.: Effects of axial induction control on wind farm energy production – A field test, *Renewable Energy*, 140, 994–1003, <https://doi.org/https://doi.org/10.1016/j.renene.2019.03.117>, 2019.
- 780 van Wingerden, J.-W., Pao, L., Aho, J., and Fleming, P.: Active power control of waked wind farms, *IFAC-PapersOnLine*, 50, 4484–4491, <https://doi.org/https://doi.org/10.1016/j.ifacol.2017.08.378>, 20th IFAC World Congress, 2017.
- von Braunbehrens, R., Vad, A., and Bottasso, C. L.: The wind farm as a sensor: learning and explaining orographic and plant-induced flow heterogeneities from operational data, *Wind Energy Science*, 8, 691–723, <https://doi.org/10.5194/wes-8-691-2023>, 2023.
- 785 Wang, C., Campagnolo, F., and Bottasso, C. L.: Identification of airfoil polars from uncertain experimental measurements, *Wind Energy Science*, 5, 1537–1550, <https://doi.org/10.5194/wes-5-1537-2020>, 2020.
- Wang, C., Campagnolo, F., Canet, H., Barreiro, D. J., and Bottasso, C. L.: How realistic are the wakes of scaled wind turbine models?, *Wind Energy Science*, 6, 961–981, <https://doi.org/10.5194/wes-6-961-2021>, 2021.